

LoCuSS: The infall of X-ray groups onto massive clusters

C. P. Haines^{1,2*}, A. Finoguenov^{3,4}, G. P. Smith⁵, A. Babul⁶, E. Egami⁷,
 P. Mazzotta⁸, N. Okabe⁹, M. J. Pereira⁷, M. Bianconi⁵, S. L. McGee⁵, F. Ziparo⁵,
 L. E. Campusano², C. Loyola²

¹*INAF - Osservatorio Astronomico di Brera, via Brera 28, 20121 Milano, Italy*

²*Departamento de Astronomía, Universidad de Chile, Casilla 36-D, Correo Central, Santiago, Chile*

³*Max-Planck-Institut für extraterrestrische Physik, Giessenbachstrae, 85748 Garching, Germany*

⁴*Department of Physics, University of Helsinki, Gustaf Hällströmin katu 2a, FI-0014 Helsinki, Finland*

⁵*School of Physics and Astronomy, University of Birmingham, Edgbaston, Birmingham, B15, 2TT, UK*

⁶*Department of Physics and Astronomy, University of Victoria, 3800 Finnerty Road, Victoria, BC, V8P 1A1, Canada*

⁷*Steward Observatory, University of Arizona, 933 North Cherry Avenue, Tucson, AZ 85721, USA*

⁸*Dipartimento di Fisica, Università degli Studi di Roma 'Tor Vergata', via della Ricerca Scientifica 1, 00133 Roma, Italy*

⁹*Department of Physical Science, Hiroshima University, 1-3-1 Kagamiyama, Higashi-Hiroshima, Hiroshima 739-8526, Japan*

18 September 2017

ABSTRACT

Galaxy clusters are expected to form hierarchically in a Λ CDM universe, growing primarily through mergers with lower mass clusters and the continual accretion of group-mass halos. Galaxy clusters assemble late, doubling their masses since $z \sim 0.5$, and so the outer regions of clusters should be replete with infalling group-mass systems. We present an *XMM-Newton* survey to search for X-ray groups in the infall regions of 23 massive galaxy clusters ($\langle M_{200} \rangle \sim 10^{15} M_{\odot}$) at $z \sim 0.2$, identifying 39 X-ray groups that have been spectroscopically confirmed to lie at the cluster redshift. These groups have mass estimates in the range $2 \times 10^{13} - 7 \times 10^{14} M_{\odot}$, and group-to-cluster mass ratios as low as 0.02. The comoving number density of X-ray groups in the infall regions is $\sim 25 \times$ higher than that seen for isolated X-ray groups from the XXL survey. The average mass per cluster contained within these X-ray groups is $2.2 \times 10^{14} M_{\odot}$, or $19 \pm 5\%$ of the mass within the primary cluster itself. We estimate that $\sim 10^{15} M_{\odot}$ clusters increase their masses by $16 \pm 4\%$ between $z = 0.223$ and the present day due to the accretion of groups with $M_{200} \geq 10^{13.2} M_{\odot}$. This represents about half of the expected mass growth rate of clusters at these late epochs. The other half is likely to come from smooth accretion of matter not bound within halos. The mass function of the infalling X-ray groups appears significantly top heavy with respect to that of “field” X-ray systems, consistent with expectations from numerical simulations, and the basic consequences of collapsed massive dark matter halos being biased tracers of the underlying large-scale density distribution.

Key words: galaxies: clusters: general – galaxies: groups: general – dark matter – large-scale structure of the Universe – X-rays: galaxies: clusters

1 INTRODUCTION

A key prediction of Λ CDM cosmological models is that structure formation occurs hierarchically, whereby dark matter (DM) halos grow via the continual accretion of lower mass systems. More massive halos thus on average form later than less massive halos. Galaxy clusters as the most massive collapsed halos form latest, doubling their masses on average since $z \sim 0.5$ (Boylan-Kolchin et al. 2009; Gao et al. 2012),

and are also the most dynamically immature. This manifests itself in 40% of local clusters showing clear substructure in their X-ray emission (Jones & Forman 1999; Chon et al. 2012; Mann & Ebeling 2012), and a higher fraction with substructure in their underlying mass distributions inferred from gravitational lensing (Smith et al. 2005; Martinet et al. 2016).

The abundances and rates of growth of galaxy clusters thus represent sensitive probes of cosmology (Voit 2005; Henry et al. 2009; Kravtsov & Borgani 2012), providing constraints on the primary cosmological parameters (Ω_m ,

* E-mail: chris.haines@brera.inaf.it

Ω_Λ , σ_8 , w_0) that are competitive with, and complementary to, those from supernovae, CMB and baryon acoustic oscillations (Allen, Evrard & Mantz 2011). While measurements of the local abundance and mass function of clusters have been used to jointly constrain the cosmic matter density Ω_m and the amplitude of density perturbations σ_8 (e.g. Schuecker et al. 2003; Planck Collaboration et al. 2014a), the rate of growth of massive clusters provides a window on the form and content of dark energy via the impact of cosmic acceleration on both structure formation and the distance-redshift relation (Mantz et al. 2010). Vikhlinin et al. (2009) compared the cluster mass function at $z\sim 0.5$ with that of present day clusters, finding an average mass growth of 75–80% for massive clusters between $z\sim 0.5$ and 0.05. This evolution maps the growth of structure and provides strong constraints on the dark energy density of the Universe with $\Omega_\Lambda=0.83\pm 0.15$ (i.e. non-zero at $>5\sigma$ significance) and its equation-of-state parameter $w_0=-1.14\pm 0.21$, assuming a constant w and a flat universe.

The merger histories of dark matter halos and the mass functions of the progenitor halos that are accreted by the primary cluster halo have been derived analytically using the extended Press-Schechter formalism (Bond et al. 1991; Bower 1991; Lacey & Cole 1993) and through cosmological N-body simulations (Lemson & Kauffmann 1999; Governato et al. 1999; Giocoli, Tormen & van den Bosch 2008) with good agreement between the two approaches. Interestingly, the *unevolved* subhalo mass function $dN(m_{sub}/M_0)/d \ln(m_{sub}/M_0)$, which parametrizes the masses of the progenitor subhalos (m_{sub}) at the time they were accreted onto the primary cluster halo, has been found to be universal, with no dependency on the primary halo mass M_0 , redshift (van den Bosch et al. 2005; Giocoli et al. 2008) or even the cosmological parameters (Zentner & Bullock 2003; Yang et al. 2011).

Collapsed dark matter halos are biased tracers of the underlying matter distribution, with the most massive halos forming from the highest peaks in the primordial linear density field. The extended Press-Schechter formalism provides robust predictions for this bias as an increasing function of peak height ν or equivalently halo mass (Mo & White 1996; Tinker et al. 2010). This leads to a systematic variation of halo mass function with large-scale (~ 10 Mpc) environment, with high-mass halos over-represented in high-density regions (Mo & White 1996), a prediction which is reproduced well in N-body simulations (Lemson & Kauffmann 1999; Governato et al. 1999; Faltenbacher, Finoguenov & Drory 2010). As clusters are preferentially located at the centres of large-scale overdensities, the mass function of halos in their surroundings, and which will subsequently be accreted onto them, should be biased towards higher mass systems.

The late assembly of clusters implies that there must be numerous group-mass systems in their outskirts in the process of being accreted. This motivates an X-ray survey covering the infall regions of a representative sample of massive clusters aimed at detecting these infalling group-mass systems and estimating their masses, with the ultimate objectives of estimating how much mass they contribute to the growth of the cluster through accretion, and whether their mass function is indeed significantly biased with respect to more typical regions of the Universe. A key advantage of de-

tecting these groups from their extended X-ray emission is that they can be unambiguously identified as massive virialized DM halos. In contrast, a purely optically-selected group sample (Ragone et al. 2004; Lemze et al. 2013) could be biased by the inclusion of non-virialized systems or chance line-of-sight projections (Pearson et al. 2017; O’Sullivan et al. 2017), the likelihood of which are dramatically increased in the vicinity of rich clusters.

Many massive clusters at $z\sim 0.2$ have been observed by *XMM-Newton* with exposure times $\gtrsim 10$ ksec, sufficient to obtain reliable temperature, gas density and mass profiles out to r_{500} and M_{500} mass estimates accurate to 10–25% (Zhang et al. 2007; Martino et al. 2014). These depths also permit the detection of galaxy groups at $z\sim 0.2$ down to masses of $\sim 2-3\times 10^{13}M_\odot$. While the ICM of the primary cluster is usually only detectable out to $\sim r_{500}$, the 30 arcmin field-of-view of *XMM-Newton* provides coverage out to $\sim 1.5-2.0r_{200}$ and enabling infalling groups in the cluster outskirts to be detected.

In this article we present a search for X-ray groups in existing *XMM-Newton* X-ray observations targetting 23 massive clusters at $z\sim 0.2$ from the Local Cluster Substructure Survey (LoCuSS), for which highly-complete stellar mass limited optical spectroscopy is available from the Arizona Cluster Redshift Survey (ACReS; Haines et al. 2013, 2015, Pereira et al. in preparation).

With this *XMM* group sample, we derive the mass function of galaxy groups infalling into massive clusters down to $M_{200}\sim 2\times 10^{13}M_\odot$, and estimate whether the accretion of these groups onto the clusters is sufficient to explain the expected mass growth of the clusters between $z\sim 0.2$ and the present day, or if further sources such as smooth accretion of dark matter are required. We examine the group-cluster mass ratio distribution and compare it to the unevolved subhalo mass function, whose universality is a key prediction of Λ CDM cosmological models (e.g. Giocoli et al. 2008).

We use a Λ CDM cosmology with $\Omega_M=0.27$, $\Omega_\Lambda=0.73$ and $H_0=72 h_{72} \text{ km s}^{-1} \text{ Mpc}^{-1}$.

2 THE CLUSTER SAMPLE, XMM DATA AND CONSTRUCTION OF THE GROUP CATALOGUE

2.1 The primary cluster sample

The primary cluster sample for this study consists of all 23 X-ray luminous clusters within LoCuSS for which there is *both* high-quality *XMM-Newton* X-ray data *and* extensive spectroscopic coverage of cluster galaxies out to $\sim 3r_{200}$ from ACReS to identify the most luminous member galaxies within the group and securely confirm its redshift.

LoCuSS is a systematic multi-wavelength survey of ~ 100 X-ray selected ($L_X \geq 2\times 10^{44} \text{ erg s}^{-1}$) massive clusters at $0.15 \leq z < 0.30$, drawn from the *ROSAT* All Sky Survey catalogues (RASS; Ebeling et al. 1998, 2000; Böhringer et al. 2004). The ACReS subsample consists of the first batch of 30 clusters having wide-field optical imaging out to the virial radii from Subaru/Suprime-Cam and *Hubble Space Telescope* imaging of the cluster cores, enabling detailed mass maps combining weak- (Subaru) and strong-lensing (HST) data. All 30 systems have excellent ancillary wide-

Table 1. The primary cluster sample. Cols. (1,2) Cluster name and redshift. Col. (3) *ROSAT* 0.1–2.4 keV X-ray luminosity, except A689^a which comes from Giles et al. (2012). Col. (4) M_{200} masses from the *Chandra-XMM* analysis of Martino et al. (2014) for the high- L_X cluster sample, extending the mass profiles out to r_{200} , except for A665 and A2218^c which come from Haines et al. (2013). Col. (5) Weak lensing M_{200} estimates from Okabe et al. (2016), except for A665, A689 and A2218^d whose mass estimates come from Pedersen & Dahle (2007); Okabe et al. (2010); Mahdavi et al. (2013).

Cluster Name	z	L_X (10^{44} erg/s)	$M_{200,X}$ ($10^{14} M_\odot$)	$M_{200,WL}$ ($10^{14} M_\odot$)
Abell 68	0.251	9.473	17.09 ± 6.45	9.24 ± 1.74
Abell 115N	0.192	8.895	6.24 ± 1.18^b	9.78 ± 3.22
Abell 209	0.209	6.289	8.71 ± 1.74	17.71 ± 2.90
Abell 267	0.229	8.569	9.28 ± 2.83	8.29 ± 1.56
Abell 291	0.196	4.883	4.16 ± 0.73	7.82 ± 2.01
Abell 383	0.189	4.559	4.46 ± 1.20	7.26 ± 1.65
Abell 611	0.286	8.855	10.66 ± 1.67	12.82 ± 2.52
Abell 665	0.183	9.837	11.71 ± 2.79^c	12.11 ± 6.83^d
Abell 689	0.278	1.812 ^a	4.34 ± 0.45	1.82 ± 0.90^d
Abell 697	0.282	10.57	21.28 ± 4.34	13.53 ± 3.49
Abell 963	0.204	6.390	8.92 ± 2.01	9.90 ± 1.79
Abell 1689	0.185	14.07	14.93 ± 3.69	15.25 ± 2.17
Abell 1758N	0.279	7.514	18.21 ± 3.59	8.17 ± 1.98
Abell 1763	0.232	9.317	14.50 ± 3.18	23.50 ± 4.25
Abell 1835	0.252	24.48	21.46 ± 5.68	14.01 ± 2.43
Abell 1914	0.167	10.98	10.70 ± 2.41	12.12 ± 2.44
Abell 2218	0.173	5.554	6.73 ± 1.60^c	7.49 ± 1.99^d
Abell 2219	0.226	12.73	21.22 ± 4.94	14.01 ± 2.71
Abell 2390	0.229	13.43	22.13 ± 7.11	14.72 ± 2.49
RXJ 1720	0.160	9.573	9.12 ± 3.81	7.26 ± 2.37
RXJ 2129	0.234	11.66	7.19 ± 0.86	6.51 ± 2.03
ZwCl 2089	0.235	6.786	2.67 ± 0.35	3.40 ± 1.39
ZwCl 7160	0.257	8.411	6.02 ± 1.37	6.14 ± 2.84

field, multi-wavelength data including near-infrared imaging with UKIRT/WFCAM (J, K ; $52' \times 52'$), *Spitzer*/MIPS $24\mu\text{m}$ and *Herschel*/PACS+SPIRE far-infrared photometry over $25' \times 25'$ fields (Haines et al. 2010; Smith et al. 2010). The L_X distribution of the ACREs subsample is statistically indistinguishable from the parent volume-limited sample of *ROSAT* clusters (Okabe et al. 2010). Of the 30 clusters covered by ACREs, 23 have existing *XMM-Newton* X-ray data suitable for detecting group-mass systems at the redshift of the cluster. These 23 systems form our primary cluster sample and are listed in Table 1.

Twenty out of the 23 clusters form part of the volume-limited “high- L_X ” LoCuSS sub-sample of 50 systems with $L_X(0.1\text{--}2.4\text{ keV})/E(z) \geq 4.2 \times 10^{44} \text{ erg s}^{-1}$, $-25^\circ < \delta < +65^\circ$ and $n_H \leq 7 \times 10^{20} \text{ cm}^{-2}$ of Okabe et al. (2013, 2016) and Martino et al. (2014). Martino et al. (2014) extracted gas density and de-projected temperature profiles for each “high- L_X ” cluster from the same *XMM* images analysed here, and derived total gravitational mass profiles and M_{500} masses assuming hydrostatic equilibrium. These mass profiles were extended out to r_{200} producing the $M_{200,X}$ mass estimates used here (Col. 4), and have mean mass uncertainties $\langle dM_{200}/M_{200} \rangle = 0.238$ (0.093 dex). These uncertainties are almost double those reported by Martino et al. (2014) for the M_{500} masses (0.052 dex), due to the need to extrapolate the mass profiles beyond r_{500} , but the

ratios between these two masses vary little between systems, $(M_{500}/M_{200}) = 0.648 \pm 0.094$. These 20 clusters also have updated weak-lensing mass measurements from Okabe et al. (2016) (Col. 5) that are fully consistent on average with our X-ray mass estimates (Smith et al. 2016), with geometric mean mass ratio $\langle M_{200,X}/M_{200,WL} \rangle = 0.985 \pm 0.106$.

Of the remaining three clusters, two (A665 and A2218) were only excluded from the high- L_X sample due to their declination ($\delta \sim +66^\circ$), and we take their X-ray mass estimates ($M_{200,X}$) from Haines et al. (2013). These are based on fitting the phenomenological cluster models of Ascasibar & Diego (2008) to a series of annular spectra extracted from deep *Chandra* data for each cluster (Sanderson & Ponman 2010). The *ROSAT* L_X estimate of the final cluster Abell 689 satisfied our high- L_X selection and it was included in the ACREs sample of 30 clusters. It was excluded from the “high- L_X ” sample of Martino et al. (2014) however, as the *Chandra* analysis of Giles et al. (2012) showed that its X-ray emission is dominated by a central BL Lac, and after excluding this central point source, the L_X from the extended cluster emission falls below the LoCuSS survey limit. ACREs does confirm A689 as a cluster (with 338 members; Haines et al. 2015), and we estimate its mass from its updated L_X using the same $M_{200} - L_X$ relation (Leauthaud et al. 2010) as used later for our *XMM*-detected groups (§2.4; Eq. 1).

A115 is a complex cluster merger with two approximately equal mass components A115N and A115S (Okabe et al. 2010; Gutierrez & Krawczynski 2005). A115N is more X-ray luminous than A115S (Forman et al. 1981), and so we take A115N as our primary cluster, while Martino et al. (2014) only measured the mass of A115S. For consistency, we derive the $M_{200,X}$ values for both A115N and A115S from the L_X estimates obtained in our analysis of the *XMM* data (§ 2.2), using Eq. 1 (§ 2.4).

2.2 Detecting extended sources in the XMM data

The details of the *XMM-Newton* observations and initial data reduction are summarized in Martino et al. (2014). After removal of energies affected by instrumental lines (as in Finoguenov et al. 2007), the 0.5–2 keV band images from the pn and MOS detectors are in-field background subtracted and co-added. To detect and identify extended emission from X-ray groups, the 0.5–2 keV band image for each cluster is then decomposed into unresolved and extended sources, using the wavelet scale-wise decomposition and reconstruction technique of Vikhlinin et al. (1998), employing angular scales from 8–64”. Similarly to Finoguenov et al. (2009, 2010, 2015) point sources in the *XMM* images are detected using the scales of 8” and 16” down to a wavelet significance of 4σ . The full flux of each detected point source is reconstructed using the *XMM* PSF model and removed from the image, following Finoguenov et al. (2009).

Having removed point sources, we apply the extended source search algorithm, applying the wavelet detection at 32” and 64” scales, and generating a noise map corresponding to the 32” scale against which the extended flux in the reconstructed image is tested for significance. We consider extended sources of X-ray emission as those detected above a 4σ threshold in the wavelet analysis, relative to the level of background fluctuations. The primary target of the obser-

vations (LoCuSS clusters) has been automatically detected as a part of this procedure. The flux measurements of each detected source are made within elliptical apertures, forcing SExtractor to describe the wavelet image as it is. The extent of the emission is traced by the wavelet routine down to 1.6σ . At the depths of these *XMM* observations, the actual signal-to-noise ratio (SNR) of the detected sources extend down to $\sim 2\sigma$, as both the contribution of the source flux to the noise is non-negligible and the flux extraction extends to areas where the source significance is just 1.6σ over the background level.

2.3 Determination of X-ray group redshifts

The optical counterparts of extended X-ray sources were identified using the combination of deep optical imaging and extensive spectroscopic data (ACReS), for which we have complete coverage over all 23 *XMM* fields. Each cluster was observed with Suprime-Cam ($34' \times 27'$ field-of-view) on the 8.2m Subaru telescope to perform the weak lensing analysis of Okabe et al. (2010, 2013, 2016). Typical observations consisted of two bands (V, i) with 30–40 min exposure times and FWHM $\sim 0.7''$, providing high-quality photometry down to $i_{AB} \sim 26$. The Arizona Cluster Redshift Survey (ACReS; Haines et al. 2013, 2015) observed all 23 clusters in our sample with Hectospec, a 300-fiber multi-object spectrograph with a 1-degree diameter circular field of view that is installed on the 6.5m MMT telescope. Target galaxies were primarily K -band selected down to a limit of $m_K^*(z_{cl}) + 2.0$ to produce an approximately stellar mass-limited sample down to $\mathcal{M} \sim 1.5 \times 10^{10} M_\odot$, with a $J-K$ colour selection used to efficiently target galaxies at approximately the redshift of the primary cluster (Haines et al. 2009a,b, 2013), irrespective of their star-formation history (i.e. with no bias towards red sequence or star-forming galaxies). We achieve spectroscopic completeness levels of $\sim 80\%$ for $M_K < -23.10$ ($M_K^* + 1.5$) cluster galaxies within the 23 *XMM* fields.

For each X-ray source, contours of the extended X-ray emission are overlaid on the Subaru optical images. In many cases there is a clear dominant early-type galaxy located near the centre of the X-ray emission, which we take to be the central group galaxy. We have a spectroscopic redshift of this galaxy for all the candidate $z \lesssim 0.4$ groups. Further group members are then sought as fainter galaxies with redshifts within 1000 km s^{-1} of the central galaxy, located within 2–3 arcmin. In cases where no dominant central galaxy is visible, we seek at least two galaxies within 1–2 arcmin of the X-ray centre with redshifts within 1000 km s^{-1} of each other. The group redshift is taken to be the mean redshift of its member galaxies. More details of the process to determine group members is given in Bianconi et al. (2017).

We are able to identify every single extended X-ray source detected at $\text{SNR} > 6.0$ as a galaxy group with known redshift, comprising 32 X-ray groups at redshifts 0.06–0.67 in addition to the targetted primary clusters. At lower significance levels (mostly at $< 3\sigma$), we find a number of the “extended” X-ray sources to be centred on background QSOs, some of which had been previously identified as X-ray point sources in *Chandra* imaging (Haines et al. 2012). Most of these QSOs had spectra having been observed as part of ACReS strategy to target all mid-infrared bright sources ($f_{24} > 1 \text{ mJy}$), including those unresolved in our K -

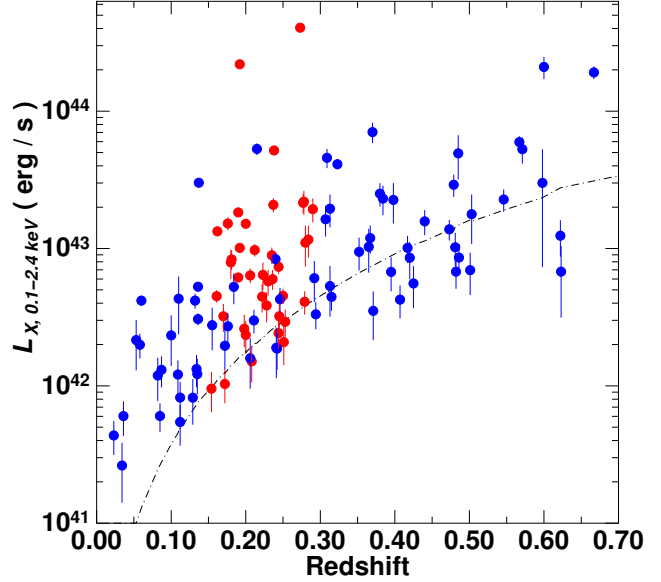


Figure 1. X-ray luminosity-redshift sampling of all the galaxy groups detected in the *XMM* images with a confirmed spectroscopic redshift. Those galaxy groups at the redshift of the primary cluster in the same *XMM* image are indicated in red, while blue points mark the remaining “isolated” galaxy groups. The dot-dashed curve indicates a flux threshold of $10^{-14} \text{ erg s}^{-1} \text{ cm}^{-2}$.

band imaging, resulting in a $24\mu\text{m}$ -selected sample of QSOs (Xu et al. 2015a,b).

As the significance of the extended X-ray source declines, the fraction for which we find no likely counterpart in the optical images starts to increase until for $2.5 < \text{SNR} < 3.0$ $\sim 40\%$ of X-ray sources remain unidentified. The bulk of these unidentified sources are likely confused low-luminosity AGN (Finoguenov et al. 2007) which are not detected on the small ($8\text{--}16''$) scales. There are no galaxies that satisfy the ACReS target selection criteria within 1 arcmin of any of these unidentified X-ray sources. In other words, we do not expect to have missed identifying any $z < 0.3$ groups due to incomplete spectroscopy.

Over the 23 *XMM* fields, excluding the primary clusters, we identify a total of 91 X-ray groups above a SNR limit of 3.0, with redshifts in the range 0.02–0.67. Ninety of these have at least one member with a spectroscopic redshift. The remaining X-ray source is centred on a compact clump of red galaxies with $J-K$ colours consistent with the group being at $z \sim 0.6$. Figure 1 shows the distribution of these 90 groups in the L_X versus redshift plane. X-ray groups that are at the same redshift as the central cluster in their *XMM* field are indicated in red, and can be typically detected down to $L_X(0.1\text{--}2.4 \text{ keV}) \sim 2 \times 10^{42} \text{ erg s}^{-1}$.

2.4 Estimation of the X-ray group masses

Using the knowledge of the group’s redshift, the global properties (L_X) of the groups are determined based on the detected flux within the aperture and estimating the total flux, based on the correspondence between the fraction of the r_{500} covered by the aperture and the group surface brightness profile, as described in Finoguenov et al. (2007). For most groups, the detection of their X-ray emission extends

Table 2. The *XMM* sample of infalling galaxy groups. The complete table of groups will appear in the final published version. Cols. (1,2) IAU name and short ID of X-ray group. Cols. (3,4) Coordinates of the centroid of the group’s X-ray emission (α, δ). Col. (5) Mean redshift of group members. Col. (6) Rest-frame X-ray luminosity of the group in the 0.1–2.4 keV band. Col. (7) Estimate of the cluster mass M_{200} in units of $10^{13} M_{\odot}$. Col. (8) Signal-to-noise ratio of the X-ray detection. Col. (9) Projected distance of group from the primary cluster centre in units of r_{200} . Col. (10) Flag indicating whether the group contains a dominant central galaxy (BGG) or not. Col. (11) Number of spectroscopically confirmed group members.

IAU Name	Group	Right	Declination	$\langle z \rangle$	L_X	M_{200}	SNR	$\frac{r_{proj}}{r_{200}}$	BGG	N_z
XMMU	ID	(J2000)	(J2000)		(0.1–2.4 keV)	($10^{13} M_{\odot}$)			Y/N	
J013137.0-134501	A209-g10	01:31:37.04	-13:45:01.9	0.20034	2.35 ± 0.62	3.03 ± 0.68	3.8	1.020	Y	2
J101640.1+385443	A963-g10	10:16:40.13	+38:54:43.0	0.20129	15.14 ± 1.12	10.00 ± 1.52	13.5	1.012	Y	21
J133210.6+503031	A1758-g7	13:32:10.67	+50:30:31.5	0.27903	4.09 ± 0.80	4.06 ± 0.77	5.1	0.643	Y	18
J215309.4+174224	A2390-g1	21:53:09.47	+17:42:24.9	0.22184	4.46 ± 1.04	4.49 ± 0.93	4.3	0.584	Y	1

to r_{500} and no correction for the aperture was made, or the applied corrections were minimal. This allows us to link the observed properties of these groups, to groups detected at similar depths in the COSMOS field (Finoguenov et al. 2007; Scoville et al. 2007) and whose X-ray luminosities were calculated in exactly the same fashion. These COSMOS X-ray groups were binned by L_X and redshift, and average total halo masses (M_{200}) derived by Leauthaud et al. (2010) for the sub-samples by stacked weak gravitational lensing, producing a $M_{200}-L_X$ scaling relation well described by a single power law.

We estimate the total M_{200} masses of our X-ray groups using the $M_{200}-L_X$ relation of Leauthaud et al. (2010) derived by performing a joint fit between the stacked COSMOS X-ray groups and ten high-mass clusters from LoCuSS with analogous X-ray and weak-lensing data (all ten are within our sample of 23). The resulting single power law relation

$$\frac{\langle M_{200} E(z) \rangle}{M_0} = A \left(\frac{\langle L_X E(z)^{-1} \rangle}{L_{X,0}} \right)^{\alpha} \quad (1)$$

with $M_0 = 10^{13.70} h_{72}^{-1} M_{\odot}$, $L_{X,0} = 10^{42.70} h_{72}^{-2} \text{erg s}^{-1}$, power-law index $\alpha = 0.64 \pm 0.03$ and $\log_{10}(A) = 0.03 \pm 0.06$, holds over two decades in mass, $M_{200} \sim 10^{13.5} - 10^{15.5} M_{\odot}$. Allevalo et al. (2012) find that the observed bias of these COSMOS X-ray groups as measured through the projected auto-correlation function is consistent with that predicted from the group masses derived via the above relation. This relation produces group masses which are always within 20% of those resulting from the $M-L_X$ scaling relation of Lovisari, Reiprich & Schellenberger (2015), whose *XMM-Newton* analysis derived total masses for 20 local groups assuming hydrostatic equilibrium. The mass scatter at fixed L_X is expected to be 0.15 dex (Kettula et al. 2015; Lovisari et al. 2015).

2.5 A catalogue of X-ray groups falling into massive clusters

X-ray groups which are infalling into the primary clusters are identified from their projected cluster-centric radii and redshifts as those located within the “trumpet”-shaped caustic profile enclosing those galaxies identified as cluster members by Haines et al. (2013). In total 39 of our X-ray groups were identified as being within the caustics of the primary cluster. The full list of infalling X-ray groups is presented in

Table 2, including their positions, redshifts, X-ray luminosities, mass estimates, whether they have an obvious central dominant galaxy (Brightest Group Galaxy or BGG) or not, and the number of spectroscopically-confirmed members. These groups all have at least one spectroscopic member, and indeed 31/39 have ≥ 7 members. The median number of spectroscopic members is nine. The velocity dispersions of these groups, as estimated using the gapper method (Beers et al. 1990), lie in the range 150–650 km s^{-1} .

Figures 2–5 show the 0.5–2.0 keV band X-ray images of Abell 1763, Abell 1835, Abell 963 and Abell 1758N, smoothed with a Gaussian kernel of width $12''$ after removing point sources. These enable the extended X-ray emission from groups in the outskirts of the cluster and in the background to be identified. Each X-ray detected group with confirmed redshift is labelled along with its M_{200} mass estimate.

The X-ray emission from Abell 1763 extends significantly in the WSW direction (as seen previously by Zhang et al. 2007, Fig. B.6), including two sub-peaks that are identified as $\sim 10^{14} M_{\odot}$ groups. Both of these peaks are close to extremely massive passive galaxies with $\mathcal{M} \sim 10^{11.6} M_{\odot}$, featureless bulges and the extended diffuse envelopes characteristic of BCGs. Two more groups with masses $5-7 \times 10^{13} M_{\odot}$ lie along the same axis, but in the opposite direction (ENE), notably directly towards Abell 1770, some 13 Mpc distant, and within the filament of star-forming galaxies previously detected as feeding Abell 1763 along this axis (Fadda et al. 2008; Edwards et al. 2010). Again the centres of X-ray emission from both groups are located close to massive passive galaxies.

Abell 1835 is a classic relaxed cool-core cluster, as demonstrated by its regular circular surface brightness contours, and the most luminous cluster in the ROSAT Brightest Cluster Sample (Ebeling et al. 1998). At larger radii (0.5–1.0 r_{200}) four X-ray groups are identified with masses $2.7-6.1 \times 10^{13} M_{\odot}$. The two most massive groups were previously identified in the *XMM* data by Pereira et al. (2010) and in *Chandra* data by Bonamente et al. (2013), who measured temperatures of 2.7 and 2.1 keV for the pair. The X-ray peaks are centred on massive passive galaxies with $\mathcal{M} \sim 10^{11.3} M_{\odot}$. The finding of numerous groups in the infall regions of A1835 can explain its velocity dispersion profile which remains flat at 1500 km s^{-1} out to 2 Mpc and significant substructures detected by the Dressler-Shectman test

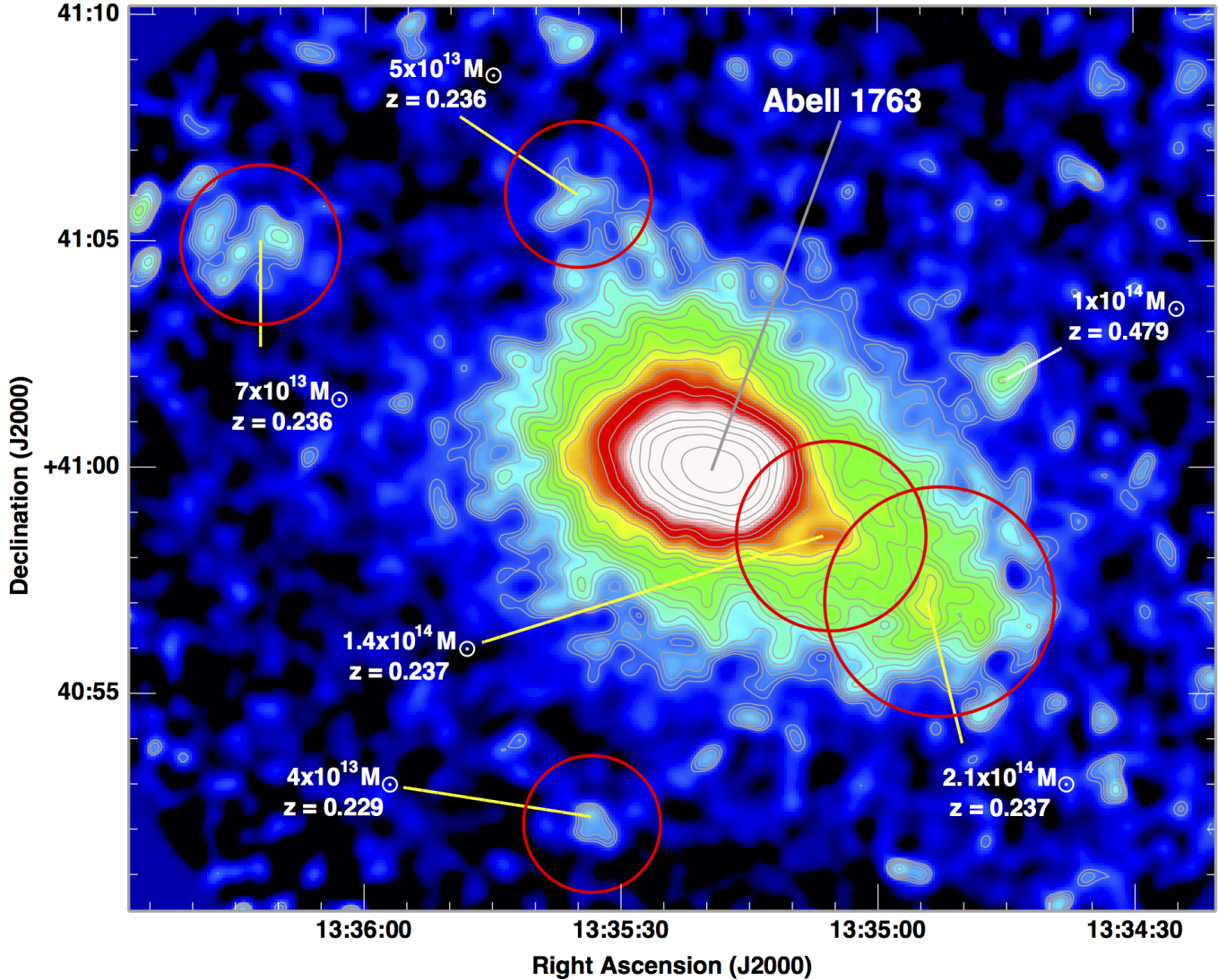


Figure 2. Extended X-ray emission from Abell 1763. All spectroscopically confirmed X-ray groups are indicated and labelled by their redshift and estimated M_{200} value. Those groups which are infalling into Abell 1763 are marked by red circles of diameter r_{200} .

(Czoske 2004). It also demonstrates how the core of a cluster may behave as a relaxed system (Smith et al. 2005), while on larger scales it is strongly disturbed due to the presence of infalling groups.

Abell 963 has been classified as a relaxed cluster based on the joint HST strong-lensing and X-ray analysis of Smith et al. (2005), although it lacks the strong cool core of A1835. The *XMM* maps again reveal significant sub-structure on large scales, with three infalling groups identified. While two are relatively poor systems ($M_{200} \sim 2\text{--}3 \times 10^{13} M_{\odot}$, the third is a massive group with $M_{200} = 1.0 \times 10^{14} M_{\odot}$, located at a projected distance of $1.0 r_{200}$ from A963. A Subaru *I_C* image centred on the group is shown in Fig. 6 with the known group members labelled. The X-ray emission (*magenta contours*) is centred on a massive passive galaxy ($\mathcal{M} \sim 10^{11.2} M_{\odot}$) which dominates the group. The BUDHIES team carried out an ultra-deep HI survey of Abell 963 and its environs, revealing that galaxies within the most massive X-ray group are strongly deficient in HI, relative to the lower mass groups and the infall regions of the cluster, and pro-

viding evidence of the impact of pre-processing on galaxies in infalling groups, stripping their gas contents and quenching star-formation before they are accreted into the cluster (Jaffé et al. 2016).

Abell 1758 is a well known double cluster system with two distinct clusters (A1758N and A1758S) separated by 8 arcmin (Rizza et al. 1998) in the plane of the sky (or 2 Mpc at $z=0.279$). Both A1758N and A1758S are undergoing major mergers, with *Chandra* imaging of A1758N revealing two remnant cores separated by 800 kpc and shock fronts (David & Kempner 2004). Our *XMM* analysis has revealed a further sub-structure within this complex system, a $4 \times 10^{13} M_{\odot}$ group that lies 6 arcmin (1.5 Mpc) ESE from A1758N and at the same redshift ($z=0.279$). The X-ray emission is centred on a compact clump of four group members, including the BCG (Fig 7), with many more group galaxies in the vicinity.

Figures 8 and 9 show two examples of our poorest infalling X-ray groups, A209-g10 and A2390-g1. In the former, the X-ray emission is centred on an obvious dominant group galaxy ($\mathcal{M} \sim 10^{11.2} M_{\odot}$), with a nearby second bright

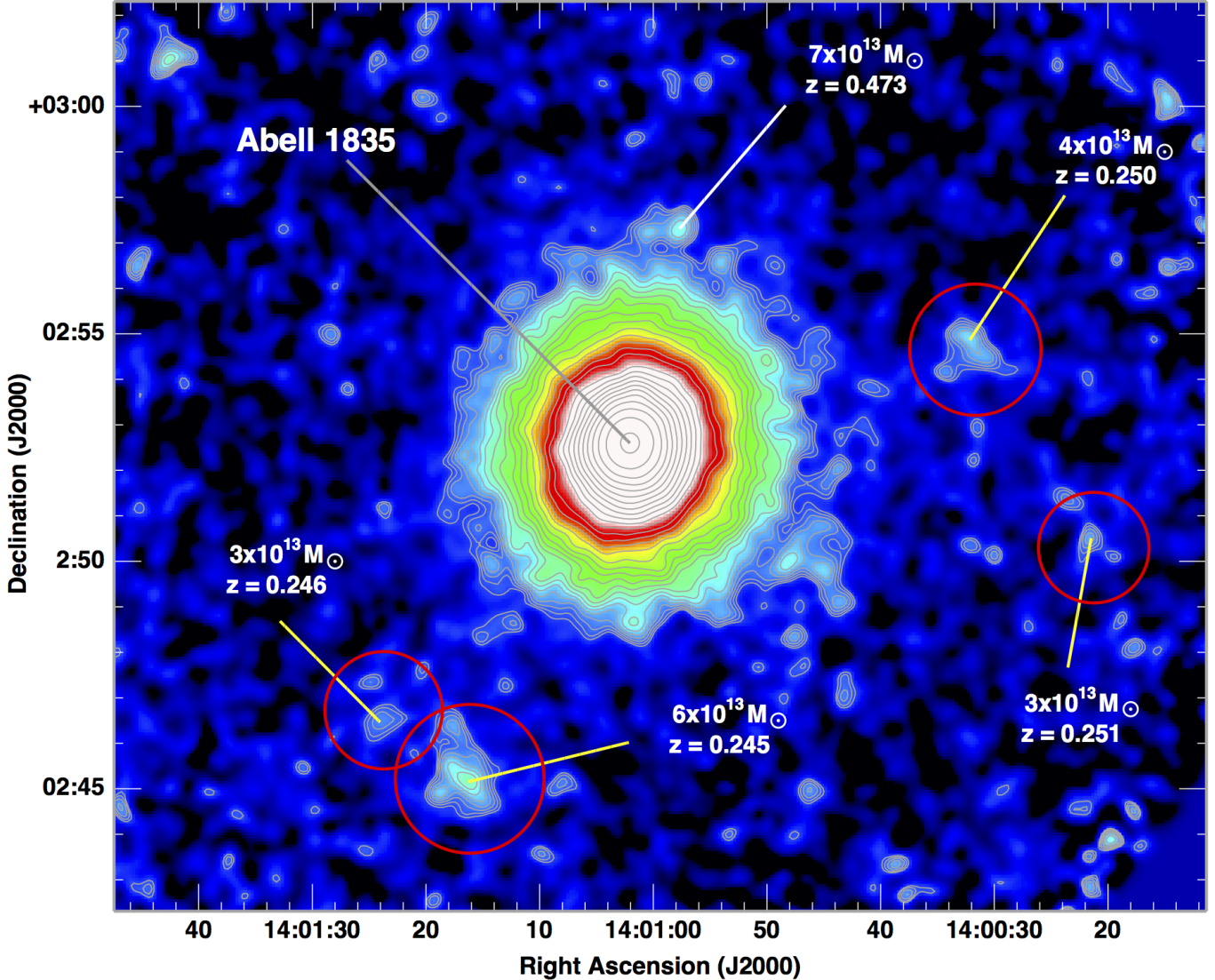


Figure 3. Extended X-ray emission from Abell 1835. All spectroscopically confirmed X-ray groups are indicated and labelled by their redshift and estimated M_{200} value. Those groups which are infalling into Abell 1835 are marked by red circles of diameter r_{200} .

galaxy within 400 km s^{-1} . In the latter, there is only one bright galaxy located within the X-ray contours, a massive ($M \sim 10^{11.0} M_{\odot}$) passive galaxy. In both cases, the association of the X-ray emission with the group galaxies appears robust and unambiguous.

2.6 A comparison sample of galaxy groups around clusters in the Millennium simulation

To understand the fates of the infalling X-ray groups, estimate the mass completeness of the *XMM* observations and to compare our results to predictions from Λ CDM cosmological models, we have created a comparison sample of galaxy groups in the vicinity of the 75 most massive clusters ($M_{200} > 4.0 \times 10^{14} h^{-1} M_{\odot}$ at $z=0.0$) from the Millennium simulation (Springel et al. 2005), a cosmological dark matter simulation covering a $(500 h^{-1} \text{ Mpc})^3$ volume. Following Haines et al. (2015) we have extracted dark matter halos with $M_{200} > 10^{13} h^{-1} M_{\odot}$ from the MPA Halo (MHalo)

catalogue within $20 \times 20 \times 140 h^{-3} \text{ Mpc}^3$ volumes centred on each cluster. These volumes are extended in the z -direction so that, for a distant observer viewing along this axis, all galaxy groups with line-of-sight (LOS) velocities within 5000 km s^{-1} of the cluster redshift are included, enabling projection effects to be fully accounted for and quantified. The group halo positions and velocities relative to the primary cluster halo are measured at the $z=0.21$ snapshot from the simulation, and artificial observations created assuming a distant observer along the z -axis. Those DM halos whose LOS velocities place them within the caustics defined by the cluster galaxy members used in Haines et al. (2015) are then retained to form our comparison sample of simulated infalling galaxy groups, and the $M_{200} - L_X$ scaling-relation of Eq. 1 used to predict their X-ray luminosities.

The completeness of each *XMM* image as a function of group mass is measured following the procedure outlined in Finoguenov et al. (2015), by generating simulated galaxy groups of a given mass and redshift, and the tabulation of

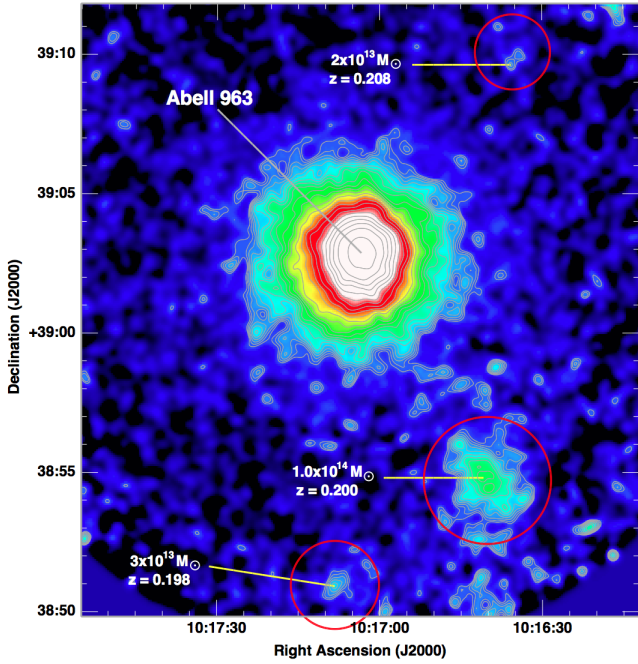


Figure 4. Extended X-ray emission from Abell 963. The three spectroscopically confirmed X-ray groups infalling into A963 are marked by red circles and labelled as in Figs. 2–3.

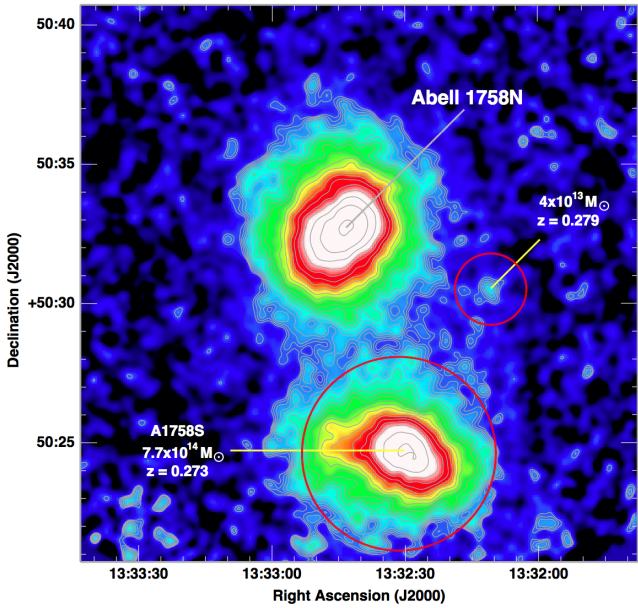


Figure 5. Extended X-ray emission from Abell 1758N. Both A1758S and the second X-ray group falling into A1758N are marked by red circles and labelled as before.

Finoguenov et al. (2007) to predict the parameters of the beta model used to describe the surface brightness profile of their X-ray emission. Unlike Finoguenov et al. (2015) we use the simulated infalling groups from the Millennium simulation to model the mass and radial distribution of groups around the cluster, rather than assume a random spatial distribution and mass distribution defined by a Λ CDM cosmological model. This step is necessary because the distri-

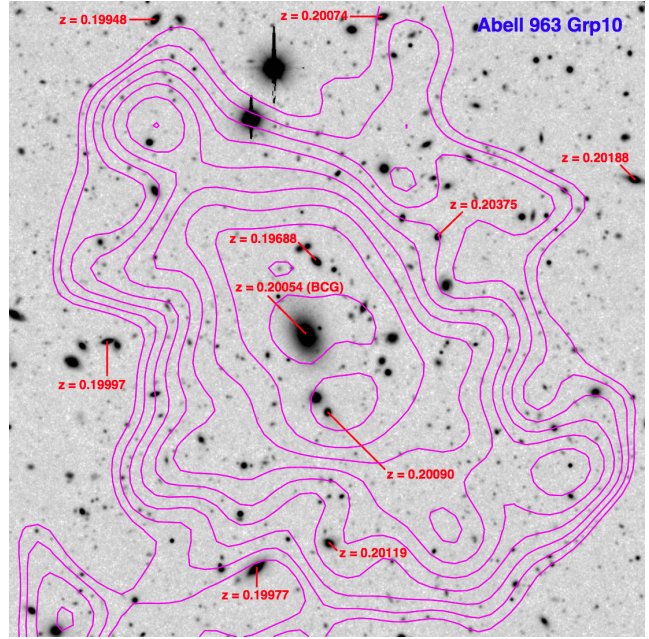


Figure 6. A $214'' \times 214''$ Subaru/SuprimeCAM I_C -band image centred on the infalling group A963-g10 ($M_{200}=1.0 \times 10^{14} M_{\odot}$). Magenta contours indicate the extended X-ray emission from the group. Spectroscopic group members are indicated in red, and their redshift reported.

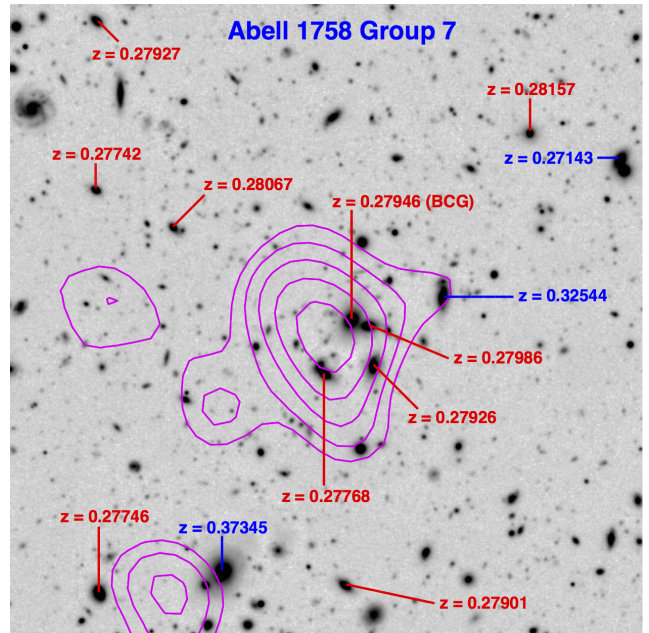


Figure 7. A $160'' \times 160''$ Subaru/SuprimeCAM R_C -band image centred on the infalling group A1758-g7 ($M_{200}=4.1 \times 10^{13} M_{\odot}$). Magenta contours indicate the extended X-ray emission from the group. Spectroscopic group members are indicated in red, and other galaxies with known redshifts indicated in blue.

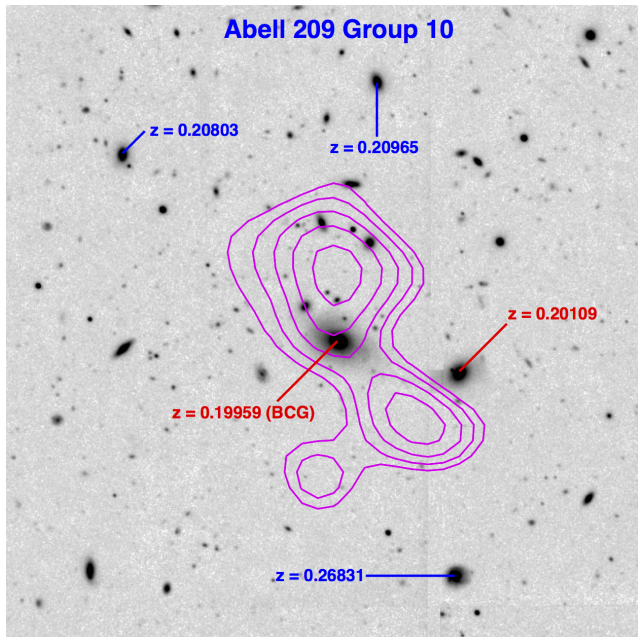


Figure 8. A $160'' \times 160''$ SuprimeCAM i -band image centred on the infalling group A209-g10 ($M_{200} = 3.0 \times 10^{13} M_{\odot}$). The two group members are indicated in red. Other galaxies with known redshifts are labelled in blue.

tribution of groups in and around clusters is not described by linear growth theory and simulations are required. The particular choice of the cosmology in the simulations is not so important, as the abundance of subhalos is not a very sensitive function of the cosmology (Taylor & Babul 2005) and the subhalo mass function scales well at any redshift as a function of the subhalo ratio to the total halo mass (Giocoli et al. 2008).

The simulated infalling X-ray groups are placed into each of the *XMM* images one at a time, and the wavelet detection algorithm applied, producing catalogues of detected simulated groups for each *XMM* cluster observation. Figure 10 plots the fraction of these simulated groups recovered by the wavelet-detection algorithm as a function of group halo mass (M_{200} ; Fig. 10a), group-cluster mass ratio (Fig. 10b) and cluster-centric radius (Fig. 10c). The blue and grey curves respectively show the recovery rates averaged over the 23 clusters, and for each individual *XMM* observation. We expect to detect $\sim 70\%$ of groups with $M_{200} \sim 5 \times 10^{13} M_{\odot}$ over the 23 *XMM* fields. The recovery rate only rises slightly to higher masses, which is partly due to some of the *XMM* observations having high backgrounds, negatively affecting the detection rate even at masses approaching $10^{14} M_{\odot}$.

The key cause of incompleteness at masses above $10^{13.5} M_{\odot}$ is revealed in Fig. 10c, where the recovery rate (blue curve) plummets from $\sim 80\%$ at $0.5 < (r_{proj}/r_{200}) < 1.0$ to just $\sim 20\%$ in the cluster cores ($r_{proj} \lesssim 0.35 r_{200}$). This is due to difficulty in distinguishing the X-ray emission from groups from the much larger emission from the primary cluster. This explains the notable absence of X-ray groups in the cluster core regions in our sample (Table 2; Fig. 11). This affects our overall mass completeness level, and the red dashed

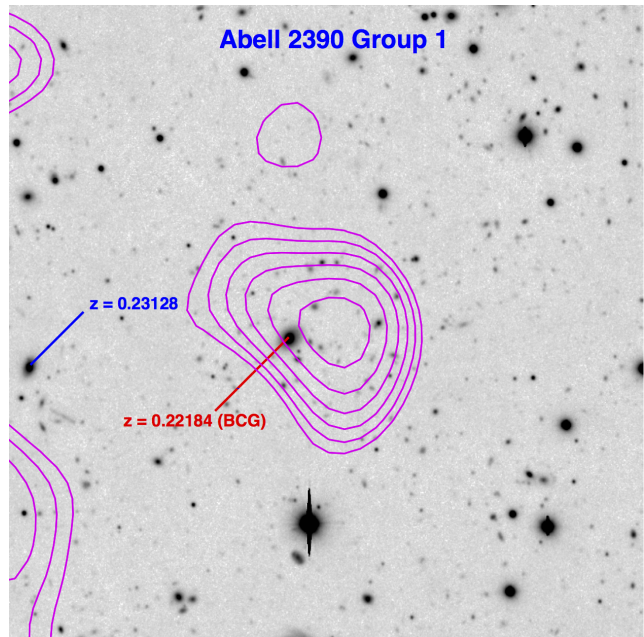


Figure 9. A $160'' \times 160''$ SuprimeCAM R_C -band image centred on the infalling group A2390-g1 ($M_{200} = 4.5 \times 10^{13} M_{\odot}$).

lines in Figs 10a,b shows the improved completeness levels after excising the cluster cores ($r_{proj} < 0.35 r_{200}$).

We also start missing X-ray groups at large cluster-centric radii due to the limited field-of-view of the *XMM* instruments, as shown by the black dashed curve in Fig. 10c. While the *XMM* data provides complete coverage inside r_{200} , the coverage fraction drops rapidly beyond $1.3 r_{200}$. Our *XMM* data is thus most efficient at detecting infalling X-ray groups at cluster-centric distances of 0.35 – $1.3 r_{200}$.

3 RESULTS

A total of 39 X-ray groups are identified across the 23 *XMM* images as being associated with the primary clusters, down to a signal-to-noise limit of 3. Six of the clusters (A267, A291, A383, A1689, RXJ2129, Z2089) have no X-ray detected groups in their infall regions, while Abell 1763 has the most with five. The numbers of groups around each cluster are consistent with the 39 groups being allocated randomly to the 23 clusters.

3.1 Spatial and velocity distribution of the infalling X-ray groups

Figure 11 shows the distribution of the 39 X-ray groups (magenta symbols) in the stacked caustic diagram. This plots the LOS velocity of each group relative to the central redshift of the primary cluster, scaled by the velocity dispersion of all cluster members within r_{200} (σ_{vel} ; taken from Haines et al. 2015), against its projected cluster-centric distance. This shows how all these groups lie within the “trumpet”-shaped region formed by the galaxies (solid grey points) that have been spectroscopically identified as members of the same 23 clusters, demonstrating that the groups are indeed associated with the clusters.

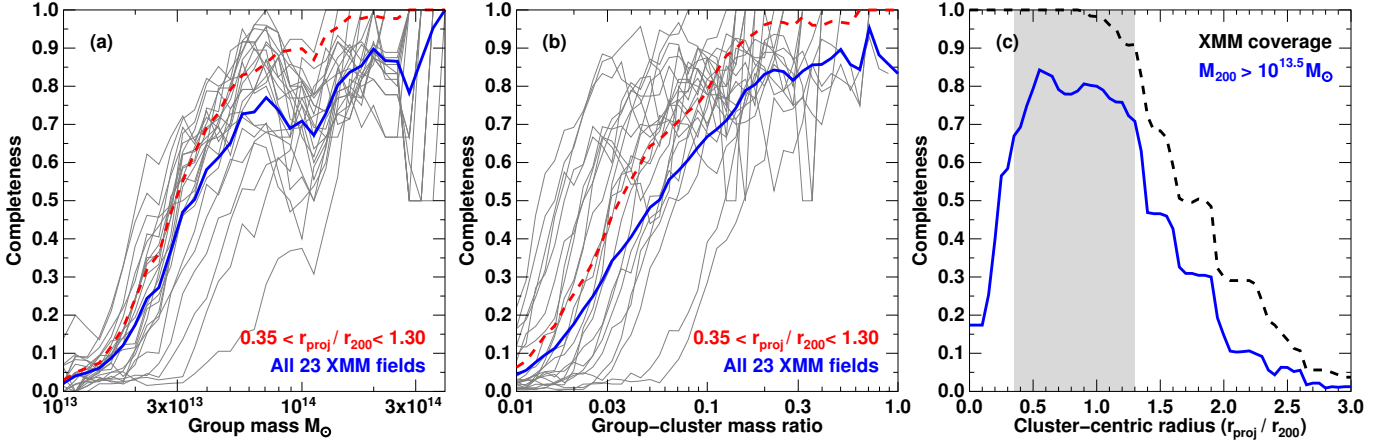


Figure 10. Fraction of simulated galaxy groups recovered by the wavelet-reconstruction detection algorithm in each of the XMM images (gray lines) as a function of group M_{200} mass (*left panel*) and group-cluster mass ratio (*central panel*). The blue curves shows the mean recovery rate averaged over all 23 clusters. The red dashed curves shows the mean recovery rate after excluding the cluster core regions with $r_{proj} < 0.35 r_{200}$ and the outer regions affected by vignetting ($r_{proj} > 1.3 r_{200}$). (*right panel*) Fraction of simulated galaxy groups with $M_{200} > 10^{13.5} M_{\odot}$ covered by the XMM imaging (black dashed curve) and recovered by the detection algorithm (blue curve) as a function of cluster-centric radius. The gray shaded region indicates the radial range over which the recoverate rate of X-ray groups within the XMM images should be highest (red dashed lines in panels a,b).

The overall distribution of relative LOS velocities for these 39 groups is shown by the histogram on the right. As discussed in detail in Haines et al. (2015), both the width and shape of the LOS velocity distribution of populations of objects in and around galaxy clusters depend strongly on when they have been (or will be) accreted into the cluster. Low LOS velocity dispersions and Gaussian distributions are indicators of virialized populations, while high LOS velocity dispersions and flat top-hat distributions are associated with objects on their first infall (Haines et al. 2015; Hikage & Yamamoto 2016).

While the velocity dispersion of the X-ray groups about the cluster redshift is marginally lower than that of the overall cluster galaxy population, $\sigma(\nu_{gr} - \nu_{cl}) = 0.86 \pm 0.08 \sigma_{\nu_{cl}}$, half of the XMM groups are located along the caustics where objects on their first infall into the clusters are expected to be found. The histogram shows an excess of groups with velocities around $-1.4 \sigma_{\nu_{cl}}$ and $+1.0 \sigma_{\nu_{cl}}$, relative to expectations from a Gaussian distribution (*blue dashed curve*), and a shortfall of groups with LOS velocities around zero. The kurtosis of the group-cluster LOS velocity distribution is negative ($\gamma = -0.82 \pm 0.36$), being inconsistent at the 2.3σ level with that of a Gaussian distribution ($\gamma = 0.0$), and closer to the value expected for a flat top-hat distribution ($\gamma = -1.2$).

The infalling X-ray groups are heavily concentrated within the radial range $0.35-1.3 r_{200}$ (vertical dashed lines) where the XMM data are predicted to be most complete (Fig. 10c), with 37/39 groups from our sample found within this range. That is not to say that we could not detect infalling X-ray groups beyond $1.3 r_{200}$. In fact, of the 52 other X-ray groups detected by XMM, but with redshifts inconsistent with that of the primary cluster, 26 were found at $r_{proj} > 1.3 r_{200}$.

Figure 12 compares the surface number density $\Sigma(r)$ distributions of the 39 infalling X-ray groups (*red points*) and the other 52 “isolated” X-ray groups (i.e. not in the vicinity of a massive cluster; *blue points*) found in the same XMM fields, as a function of projected cluster-centric radius.

The two radial distributions are markedly different. The infalling X-ray groups show a sharp peak at $0.5-0.75 r_{200}$, before dropping off rapidly at larger radii and no infalling groups beyond $1.33 r_{200}$, while the other X-ray groups in the same field show a rather flat radial distribution over $0.5-1.75 r_{200}$. In both cases, the number densities of groups drops inside $0.5 r_{200}$ and are absent within $0.25 r_{200}$, due to the inability to detect X-ray groups projected close to the cluster core in the XMM data (Fig. 10c). The upper panel shows the corresponding cumulative radial distributions of the infalling X-ray groups (*red curve*) and isolated “field” groups (*blue curve*). The infalling groups are found much closer on average to the primary cluster than the back/foreground X-ray groups. The median projected cluster-centric distance of the infalling groups is $0.71 r_{200}$, compared to $1.29 r_{200}$ for the remaining X-ray groups detected in the same XMM fields. The largest difference is seen at the virial radius, with 35/39 (90%) infalling groups having $r_{proj} < 1.02 r_{200}$, while 39/52 (75%) of the isolated groups lie at $r_{proj} > 1.02 r_{200}$. The non-parametric Mann-Whitney U-test confirms the radial distributions of the infalling and field groups to be inconsistent at the 6.0σ level.

As these other X-ray groups are not associated with the cluster, we should expect them to be uniformly distributed across the XMM images, but then be affected by the same radial selection biases as the infalling groups (Fig. 10c). The green dashed curve shows the expected cumulative radial distribution of groups assuming a uniform spatial distribution over the XMM images, and taking into account the loss of sensitivity in the cluster core regions. The fore/background X-ray groups are consistent with being randomly distributed across the XMM fields, while the infalling X-ray groups are clearly not.

The strong preference of infalling X-ray groups to lie within r_{200} can be understood in terms of the expected clustering of group-mass systems around massive clusters. The light-grey shaded histogram shows the surface number density of $M_{200} > 10^{13} M_{\odot}$ DM halos (groups) in the vicinity

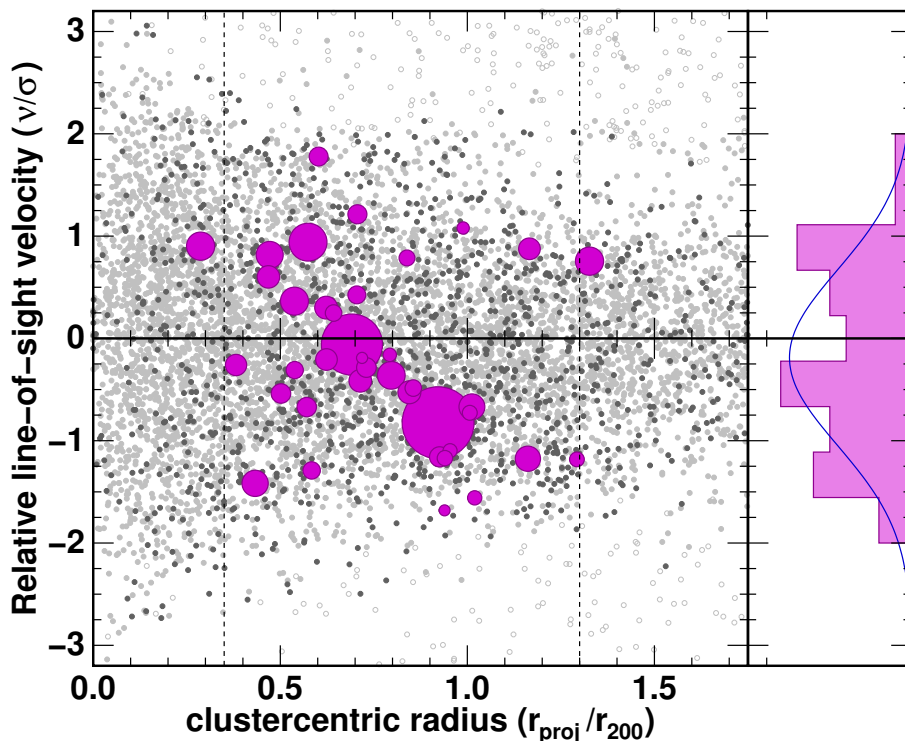


Figure 11. Stacked phase-space diagram, $(v_{los} - \langle v \rangle) / \sigma_v$ versus r_{proj} / r_{200} of the 39 XMM groups (*magenta symbols*) and member galaxies (*grey solid points*) for all 23 clusters in our sample. The size of each symbol indicates the group mass. Darker grey symbols indicating star-forming galaxies detected at $24\mu\text{m}$. Open symbols indicate field galaxies. The vertical dashed lines enclose the $0.35 \leq (r_{proj} / r_{200}) < 1.30$ region where the XMM data is most complete. The solid histogram on the right shows the distribution of relative LOS velocities for the 39 XMM groups, while the blue curve shows a Gaussian distribution with the same mean and standard deviation.

of the 75 most massive clusters from the Millennium Simulation (MS), as a function of projected cluster-centric distance. The surface number density shows a sharp peak inside $0.5 r_{200}$, before rapidly dropping to larger radii, falling six-fold by $r_{proj} \sim 2 r_{200}$. This is the predicted radial distribution of groups before accounting for observational biases, and the difficulty in detecting X-ray groups within $0.5 r_{200}$ above the much greater emission from the cluster ICM pushes the expected peak out to $0.25\text{--}0.75 r_{200}$ (*darker histogram*). The sharp increase in the projected number density of groups moving towards the cluster centre parallels that seen also for the member galaxies (Haines et al. 2015, Fig. 5), which was best fit by an NFW profile with $c_g = 3.01 \pm 0.16$ (*dashed curve*; Haines et al. 2015). Such an NFW profile also describes well the predicted radial distribution of groups (*grey histograms*) over $0.5\text{--}2.2 r_{200}$, but is inconsistent with our lack of infalling X-ray groups beyond $1.5 r_{200}$. This largely reflects the fact that clusters lie at the centres of large-scale ($\gtrsim 10$ Mpc) overdensities that extend well beyond the virial radius (Frenk et al. 1999). These large-scale overdensities are collapsing inwards towards the cluster, dragging the infalling X-ray groups and galaxies with them (Haines et al. 2015, Figs. 9,10).

3.2 The mass function of infalling X-ray groups

Figure 13 shows the mass function (MF) of the infalling X-ray groups (*red points*), after correcting for incompleteness (§2.6). The left-hand axis shows the MF in units of groups

per dex in mass per comoving Mpc^3 . The comoving volume containing the infalling group sample for each cluster is estimated as that within the redshift limits corresponding to the cluster caustics and extending over a circular area of sky of radius $1.3 r_{200}$. Summing these 23 volumes gives a grand total comoving volume of $5.9 \times 10^4 \text{Mpc}^3$.

The slope of the mass function appears to flatten off for masses below $\sim 10^{14} M_\odot$. The shape and overall normalization of the MF (in terms of groups per mass bin per cluster; right-hand axis) is consistent with that predicted by the MF of infalling galaxy groups with projected separations $< 1.3 r_{200}$ from the 75 most massive clusters in the Millennium simulation (*dot-dashed magenta curve*).

For comparison, the thick blue curve shows an estimate of the overall MF of clusters in the universe at $z \sim 0.2$, obtained by applying the same $M_{200} - L_X$ relation to the X-ray luminosity function (XLF) of Pacaud et al. (2016). This XLF is based on a flux-limited sample of the 100 brightest extended X-ray sources found in the XXL survey (Pierre et al. 2016). This is the largest programme carried out by XMM-Newton, covering a total area of 50deg^2 (412 XMM pointings) over two fields, to comparable depths (10 ksec) as those used here, with the objective of providing a statistical and representative sample of groups and clusters out to $z \sim 0.5$ (and above), suitable for constraining cosmological parameters. Most of these systems are located between $z = 0.1$ and 0.5 . The X-ray luminosities of Pacaud et al. (2016) were measured over the $0.5\text{--}2.0 \text{keV}$ spectral band, and so were first divided by a global factor of 0.59 to k-correct them to the

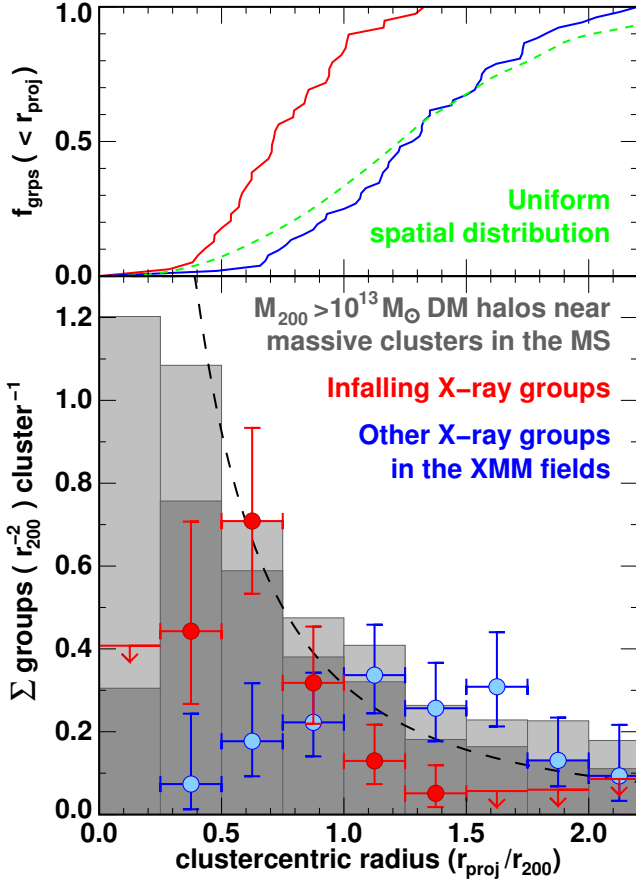


Figure 12. Composite surface number density distribution $\Sigma(r)$ of the 39 observed infalling X-ray groups (*red points*) and 52 other “isolated” field X-ray groups (*blue points*) as a function of projected cluster-centric radius (lower panel). For those radial bins containing no infalling groups, the Poisson 1σ upper limit (Gehrels 1986) is shown. The light grey shaded histogram shows the predicted number density distribution of $M_{200} > 10^{13} M_{\odot}$ groups as a function of projected cluster-centric radius around the 75 most massive clusters in the Millennium simulation at $z=0.21$. The dark shaded distribution indicates the predicted radial distribution of those groups which would be detected, applying the completeness correction of Fig. 10c. The dashed curve shows the best-fit NFW profile to the radial distribution of cluster galaxies ($c_g=3.01$; Haines et al. 2015). The upper panel shows the cumulative radial distribution $f(<r_{proj})$ of the infalling X-ray groups (*red curve*) and “isolated” X-ray groups detected in the same XMM fields. The dashed green curve indicates the predicted cumulative radial distribution if groups were uniformly distributed across the XMM images, taking into account the effects of incompleteness in the cluster cores (Fig. 10c).

0.1–2.4 keV band used here and in Leauthaud et al. (2010). The most notable difference between the “cosmic” MF and that of our infalling X-ray groups, is the overall normalization. The comoving number density of X-ray groups in the infall regions of clusters is more than an order of magnitude higher than that seen in the XXL survey volume. The “cosmic” MF has to be normalized upwards by a factor ~ 26 (*thin blue curve*) in order to predict the same overall number of $M_{200} > 10^{13.2} M_{\odot}$ groups as that observed in the XMM infalling group sample.

Moreover, over the remainder of the $0.15 \leq z < 0.30$ vol-

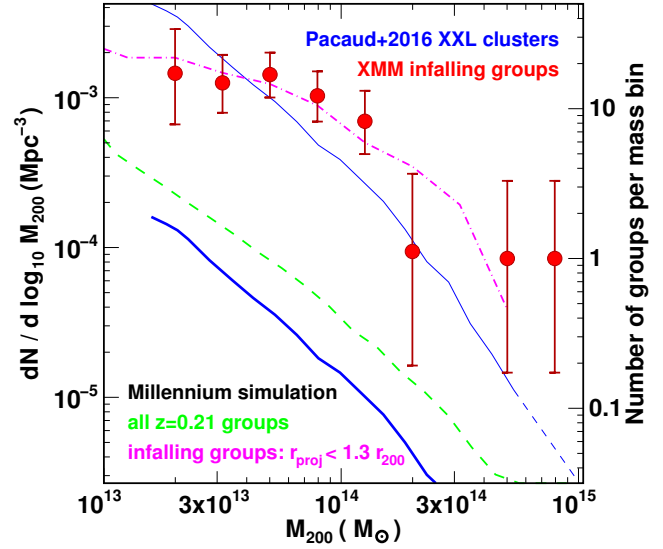


Figure 13. Mass function of the 39 XMM-detected groups with redshifts associating them with the 23 primary clusters (red solid symbols). Error bars indicate Poisson uncertainties based on Gehrels (1986). The thick blue curve indicates the mass function derived from the X-ray luminosity function of groups and clusters from the XXL survey (Pacaud et al. 2016). The thin blue curve shows the same mass function, normalized upwards by a factor 26 (see text). The dot-dashed magenta curve shows the mass function of simulated infalling galaxy groups within $1.3 r_{200}$ (projected) of the 75 most massive clusters in the Millennium simulation at $z=0.21$, while the dashed green curve indicates the $z=0.21$ halo mass function averaged over the whole Millennium simulation.

ume covered by our 23 XMM images, we detect only ten more X-ray groups above the 3σ SNR threshold, despite this volume being $5.76 \times$ larger than that confined within the redshift limits of the clusters. This corresponds to an over-abundance of X-ray groups in the cluster infall regions of a factor ~ 22 , comparable to the previous estimate, and confirming that the infall regions of clusters are $\sim 25 \times$ overdense in group-mass systems with respect to the cosmic average at that redshift.

The shapes of the two MFs also appear different. The flattening seen in the MF of the infalling X-ray groups is in marked contrast to the much steeper MF of XXL systems, which can be well described as a single power law ($N(M) \propto M^{-1.6}$) without any sign of a break. This steep, power-law form closely resembles the global MF of DM halos averaged over the full volume of the Millennium simulation at $z=0.21$ (*dashed green curve*), where no break in the MF is apparent. The clear difference in the mass functions of the X-ray groups around massive clusters presented here and of X-ray groups sampled over a large, representative volume of the Universe through the XXL survey, reproduces well the predicted effect of the overdense cluster environment on the mass function of DM halos seen within the Millennium simulation.

The apparent differences in the shape of the mass function of X-ray groups according to large-scale environment is further elucidated in Figure 14, which shows the cumulative mass fractions of X-ray groups from the XXL survey (*blue curve*) and the 39 infalling X-ray groups (*red line*),

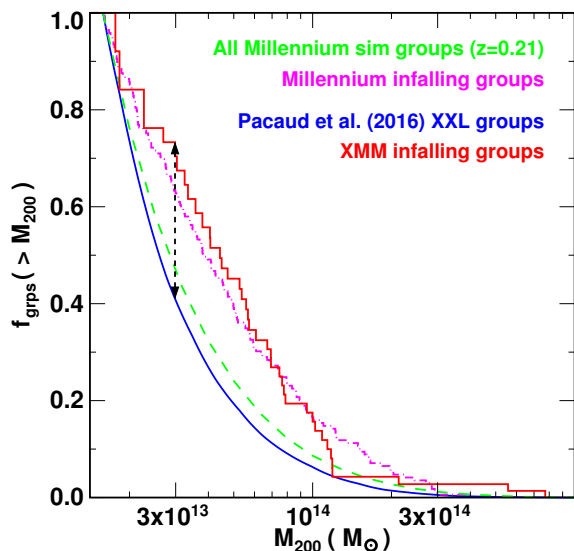


Figure 14. Cumulative mass distribution $f(>M)$ of the 39 *XMM*-detected galaxy groups (red line), X-ray groups from the XXL survey (Pacaud et al. 2016, blue curve), infalling galaxy groups around 75 massive clusters in the Millennium simulation (dot-dashed magenta line), and all $z=0.21$ DM halos with $M_{200} \geq 10^{13.2} M_{\odot}$ in the Millennium simulation (green dashed curve). The vertical dashed line indicates the maximal differences between the observed cumulative mass distributions.

as well as the corresponding DM halo populations from the Millennium simulation. Each curve presents the fraction of $M_{200} > 10^{13.2} M_{\odot}$ groups (DM halos) that are also above a given M_{200} mass, as a function of M_{200} . This confirms that the mass function of the X-ray groups found in the vicinity of massive clusters is systematically top-heavy with respect to that of the general population of X-ray groups at these redshifts from the XXL survey. A Kolmogorov-Smirnov test finds that the probability that both mass functions are drawn from the same distribution to be just 0.0006 ($D_{KS}=0.323$; maximal distance between curves is shown by the vertical black line). This corresponds to a 3.5σ result.

The systematic bias towards a top-heavy MF observed for X-ray groups around massive clusters replicates that seen in the Millennium simulation (Faltenbacher, Finoguenov & Drory 2010; Haines et al. 2015). The cumulative mass function of DM halos in the vicinity ($r_{proj} < 1.3 r_{200}$) of a massive cluster at $z=0.21$ (magenta dot-dashed curve) is found to be consistent with our observed MF for infalling X-ray groups, and top-heavy with respect to the MF of DM halos averaged across the full Millennium simulation at the same snapshot (green dashed curve). The large-scale overdensity centred on the massive cluster biases the halo mass function in its vicinity, increasing the relative contribution of higher mass halos at the expense of lower mass systems. This biasing has the effect of increasing the importance of accreting $\sim 10^{14} M_{\odot}$ systems to the mass growth of rich clusters with respect to simple predictions based on the cosmic halo mass function.

3.3 The total mass contained within infalling groups

The total mass of the 39 infalling groups detected by *XMM* is $3.77 \times 10^{15} M_{\odot}$, which after correcting for incompleteness

comes to $5.13 \times 10^{15} M_{\odot}$ in systems above $10^{13.2} M_{\odot}$, or $2.23 \times 10^{14} M_{\odot}$ for each of the 23 clusters in our sample. This corresponds to $19.5 \pm 5.1\%$ of the mean mass of the 23 primary clusters ($\langle M_{200} \rangle = 11.47 \times 10^{14} M_{\odot}$), where the uncertainty is estimated by bootstrap resampling to account for the significant cluster-to-cluster scatter.

The two most massive X-ray “groups” in Fig. 13 are Abell 1758S and Abell 115S, both of which are the lesser component of well-known double clusters undergoing major mergers (David & Kempner 2004; Gutierrez & Krawczynski 2005; Okabe & Umetsu 2008). Although nominally clusters, we include these among our infalling X-ray “groups” as they will be accreted and subsumed by the primary cluster (A1758N, A115N) in the same way. Even so, these two clusters only contribute $1.33 \times 10^{15} M_{\odot}$ between them, representing 26% of the total mass within our infalling X-ray group sample. Excluding them does not dramatically change our estimate of the amount of mass being accreted onto clusters in the form of groups.

3.4 The group-cluster mass ratio distribution

Figure 15 shows the distribution of M_{200} mass ratios between the infalling galaxy groups and the primary clusters that they are associated with (M_{gr}/M_{cl} ; red points), using the *XMM*-based $M_{200,X}$ cluster masses from Table 1. The mass-ratio distribution appears approximately consistent with a power law $dN/d \ln(M_{gr}/M_{cl}) \propto (M_{gr}/M_{cl})^{-\alpha}$ over the range 0.02–1.0 in group-cluster mass ratio, with $\alpha = 1.17_{-0.34}^{+0.28}$ (red dot-dashed line). This is in excellent agreement with the best-fit power-law index of $1.09_{-0.32}^{+0.42}$ obtained by Okabe et al. (2014) for the sub-halo mass function through a weak lensing analysis of sub-halos in the Coma cluster, and indices ~ 0.9 – 1.0 predicted by analytical models (Taylor & Babul 2005) and numerical simulations.

The black solid curve shows the *unevolved* subhalo mass function of Giocoli et al. (2008):

$$\frac{dN}{d \ln(m_{gr}/M_{cl,0})} = N_0 x^{-\alpha} \exp(-6.283x^3), \quad x = \left| \frac{m_{gr}}{\alpha M_{cl,0}} \right| \quad (2)$$

where m_{gr} is the mass of the progenitor group halo at the time of accretion, $M_{cl,0}$ is the present day mass of the descendant cluster, $\alpha=0.8$ and $N_0=0.21$. Here we assume that $M_{cl,0} = (M_{cl} + M_{gp})$, i.e. the group’s mass has been subsumed by the cluster by the present day. Jiang & van den Bosch (2014) refined the fitting function of Giocoli et al. (2008), adding in an extra power-law term to better model the unevolved subhalo mass function of halos within the Millennium simulation (blue curve).

The form and steepness of the mass-ratio distribution of infalling *XMM* groups reproduces well the unevolved subhalo mass functions of both Giocoli et al. (2008) and Jiang & van den Bosch (2014), the main difference being a systematic shortfall at most mass ratios. This is unsurprising, as we are only detecting the groups which are being accreted into the clusters at late epochs, while the functions of Giocoli et al. (2008) and Jiang & van den Bosch (2014) include the contributions of subhalos accreted at all redshifts, a significant fraction of which will have long been stripped of their X-ray emitting gas halos.

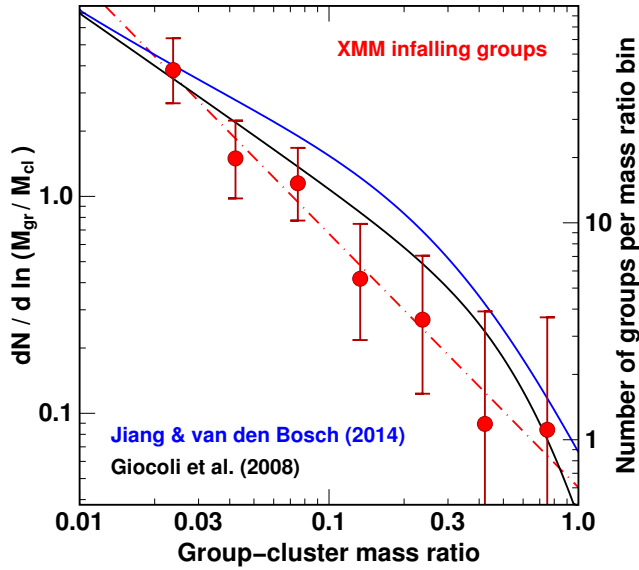


Figure 15. The distribution of the mass ratios between *XMM*-detected galaxy groups and the primary clusters, after correcting for incompleteness (red solid symbols). The best-fit power law is shown by the red dot-dashed line. The black and blue curves show the predicted *unevolved* subhalo mass functions of Giocoli et al. (2008) and Jiang & van den Bosch (2014) respectively.

3.5 Offsets between the BGG and the X-ray centroid of the infalling groups

In isolated, undisturbed galaxy groups, the central group galaxy (BGG) and the centroid of the X-ray emission should be coincident. When a group falls into a galaxy cluster, the X-ray emitting gas of the group is incrementally stripped by the ram pressure exerted by the cluster’s own X-ray emitting ICM. This causes the group’s X-ray gas to drag and thus lag behind the member galaxies, which as effectively collisionless particles. For the 32 infalling X-ray groups for which a clear BGG could be identified, we find a median separation of 65 kpc between the BGG and the X-ray centroid, with 68% of the separations in the range 28–143 kpc. These separations are consistent with those seen for infalling groups in the BAHAMAS simulation (McCarthy et al. 2017). The X-ray centroid is further away from the cluster centre than the BGG for 19/32 systems.

4 DISCUSSION

A fundamental prediction of the Λ CDM model is that galaxy clusters, as the most massive collapsed halos in the universe, form latest, doubling their mass since $z \sim 0.5$ (e.g. van den Bosch et al. 2014). As structure formation occurs hierarchically, much of this late mass growth must be achieved through the accretion of poorer clusters and group-mass systems, and so the outer regions of clusters must be replete with infalling group-mass systems. The key objective of our *XMM* survey of 23 massive clusters is to perform a simple empirical verification of the ongoing assembly of massive clusters through the accretion of groups, as predicted by Λ CDM, and to estimate the contribution of these infalling groups to the mass growth rate of the primary clusters.

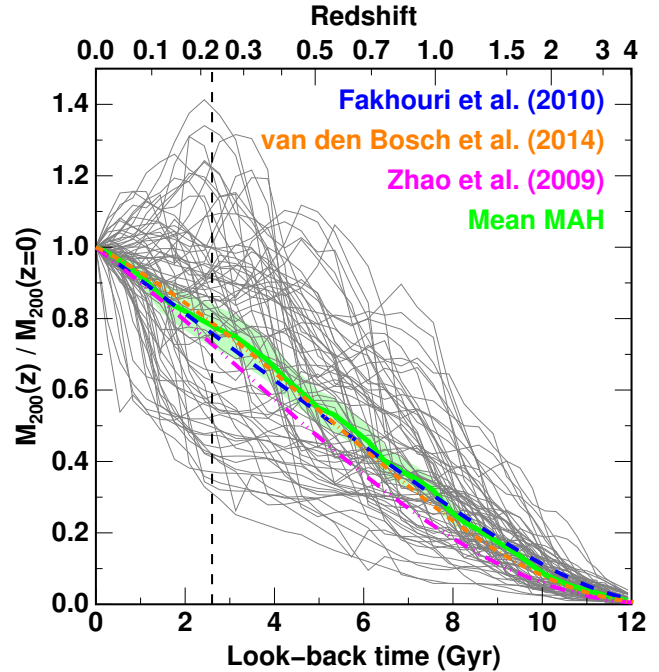


Figure 16. The mass accretion histories (MAHs) of the 75 most massive DM halos in the Millennium simulation (grey curves). The solid green curve indicates the mean MAH of these 75 halos, while the green shaded region indicates the expected 1σ range of MAHs when averaging over 23 clusters selected at random from the full sample. The dashed blue, dot-dashed orange and magenta curves indicate the mass growth for halos of present day mass $M_{200} = 10^{15} h^{-1} M_{\odot}$ predicted by Eq. 4 (Fakhouri et al. 2010), van den Bosch et al. (2014) and Zhao et al. (2009) respectively. The vertical black dashed line indicates the mean redshift ($\bar{z} = 0.223$) of the LoCuSS primary clusters and *XMM* infalling groups.

4.1 The mass assembly history of clusters

The average rates at which clusters assemble their mass through mergers and accretion as function of redshift have been investigated for a range of cosmologies using a combination of N-body simulations and Monte-Carlo realisations based on the extended Press-Schechter (EPS) framework.

McBride et al. (2009) investigated the mass accretion histories (MAHs) of DM halos from the Millennium simulation, finding that a two-parameter function of the form

$$M(z) = M_0(1+z)^{\beta} \exp(-\gamma z) \quad (3)$$

was versatile enough to accurately capture the main features of most MAHs in the simulation. They were also able to obtain a good fit to the mean mass growth rates of halos as a function of halo mass and redshift, by differentiating the above equation. Correa et al. (2015) have shown using EPS theory and the redshift dependence of the linear growth factor $D(z)$ that the mass growth of halos is well described by an exponential growth at high redshifts, while at low redshifts when dark energy dominates, the growth of density perturbations is slowed by the accelerated expansion of the Universe, necessitating an additional power-law term.

Figure 16 shows the mass accretion histories of the 75 most massive DM halos in the Millennium simulation (MS; grey curves). The main branch of the merger tree of each cluster halo is determined by identifying the most massive

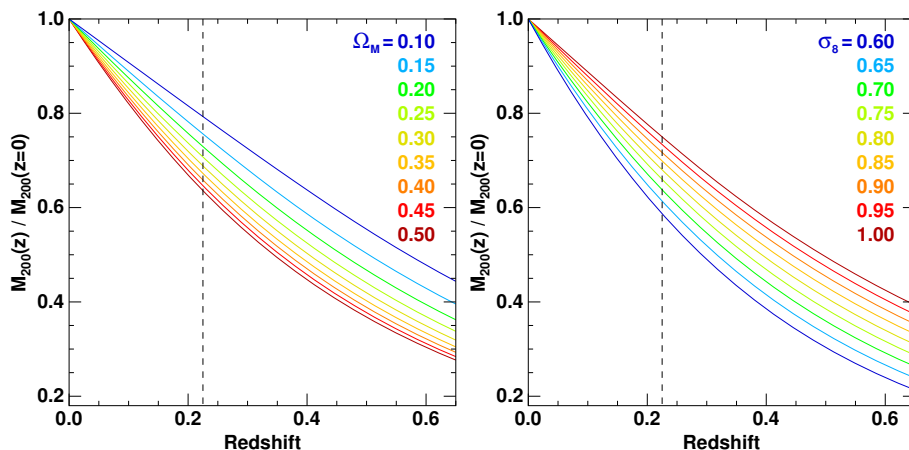


Figure 17. Average MAHs, $\langle M_{200}(z)/M_{200}(z=0) \rangle$, for halos of final mass $M_0=10^{15}h^{-1}M_\odot$ in different, flat Λ CDM cosmologies, based on the empirical models of Zhao et al. (2009). The left panel shows the effect of varying Ω_M from 0.1 to 0.5 in steps of 0.05, while the right panel shows the effect of varying σ_8 from 0.6 to 1.0 in steps of 0.05. All of the other cosmological parameters are kept fixed at the values from the Planck 2015 model. The vertical dashed line indicates the mean redshift ($\bar{z}=0.223$) of our sample of 23 clusters.

progenitor of the descendent cluster halo in the previous snapshot. The most notable feature is the large cluster-to-cluster scatter among the MAHs, with some clusters assembling more than half of their mass in the last 2 Gyr, while others were largely in place by $z\sim 0.5$ and some are appearing to be losing mass at late epochs. These mass loss events occur during major mergers, which produce first a dramatic increase in mass and a corresponding rapid increase in the velocity dispersion, followed by a slower phase of mass loss as a significant amount of mass from the secondary halo rebounds out of the primary halo and orbits beyond its r_{200} radius for 2–4 Gyr (Behroozi et al. 2015), analogously to “back-splash” galaxies.

While the individual cluster MAHs show significant stochastic variation, the mean MAH (*green curve*) shows a steady monotonic increase in mass over the last 10 Gyr. The large scatter in individual MAHs implies the need to average over many clusters to derive useful constraints on the cosmic growth of mass within clusters, and the green shaded region indicates the 1σ range in *averaged* MAHs produced by combining the growth rates of 23 clusters, selected at random from the full sample. The total M_{200} masses of a random sample of 23 MS clusters should have $77.6\pm 5.9\%$ of their present day M_{200} mass at $z=0.223$, the mean redshift of our primary clusters (*vertical dashed line*). In other words, they should grow by a further $29\pm 10\%$ between $z=0.223$ and the present day.

Using the higher-resolution Millennium II simulation, Fakhouri et al. (2010) obtained updated analytic fits to the mean mass growth rates of halos of mass M at redshift z of:

$$\langle \dot{M} \rangle_{\text{mean}} = 46.1 M_\odot \text{ yr}^{-1} \left(\frac{M}{10^{12} M_\odot} \right)^{1.1} \times (1 + 1.11z) \sqrt{\Omega_m(1+z)^3 + \Omega_\Lambda}. \quad (4)$$

The resulting mass accretion history for a cluster halo of present day mass $M_{200}=10^{15}M_\odot$ (*dashed blue curve*) is consistent with the mean MAH of the 75 most massive MS clusters. Zhao et al. (2009) derived a universal empirical model for the MAHs of DM halos, by analysis of numerous N-body simulations of a wide variety of cosmological models, which

predicts a somewhat later mass assembly for $10^{15}h^{-1}M_\odot$ halos (*dot-dashed magenta curve*) in a Millennium cosmology. van den Bosch et al. (2014) used EPS merger trees calibrated with the Bolshoi N-body simulation to derive average MAHs for halos of a given mass in any Λ CDM cosmology (*dot-dashed orange curve*).

These models all predict similar MAHs for $10^{15}h^{-1}M_\odot$ clusters, whereby they have grown at a virtually constant rate since $z\sim 1$ (Fig. 17). The MAHs of van den Bosch et al. (2014), Fakhouri et al. (2010) and Zhao et al. (2009) respectively predict mass increases of 27%, 32% and 37% between $z=0.223$ and the present day. These correspond to mass growth rates of 13–17% per Gyr for clusters at $z\sim 0.2$.

4.1.1 Dependence on cosmological parameters

The curves shown in Fig. 16 demonstrate well the expected cluster-to-cluster scatter among their MAHs. Strictly speaking they are only valid for the exact cosmological model used in the simulation. The parameters were set in the MS ($\Omega_m=0.25, \Omega_\Lambda=0.75, \sigma_8=0.90, n_s=1.0, h=0.73$) to be close to those obtained from WMAP1 (Spergel et al. 2003), but are now somewhat divergent from the current best estimates obtained from analysis of the full-mission Planck CMB data ($\Omega_m=0.308\pm 0.012, \sigma_8=0.8149\pm 0.0093, n_s=0.9677\pm 0.0060, H_0=67.81\pm 0.92$; Planck Collaboration et al. 2016).

The universal models of Zhao et al. (2009) and the EPS-based models of van den Bosch et al. (2014), allow us to investigate the dependence of the average MAHs of cluster-mass halos on the main cosmological parameters, and recalibrate the results onto the Planck 2015 cosmological model. Figure 17 shows the effect of varying Ω_m and σ_8 on the average MAHs of DM halos with present day masses $M_{200}=10^{15}M_\odot$ in flat Λ CDM cosmologies, while keeping the remaining parameters fixed to the Planck 2015 values, using the Zhao et al. (2009) code with an Eisenstein & Hu (1998) power spectrum. These confirm that both Ω_m or σ_8 have a significant affect on the MAHs of cluster-mass halos, with the rate of growth at late epochs rising with increasing Ω_m and decreasing σ_8 . In contrast, varying the tilt of the pri-

mordial power-law spectrum n_s has negligible influence on the MAHs of cluster-mass halos.

Increasing Ω_m from 0.25 (MS) to 0.308 (Planck 2015) results in a corresponding increase in the rate of growth of clusters from $z=0.223$ to the present day of 7.4%, while decreasing σ_8 from 0.90 to 0.8149 increases the growth rate by an additional 10.9%. The combined changes in moving from the MS cosmological model to that of Planck 2015 increases the late-time growth rate by 18.3%, resulting in mass growth rates for $z\sim 0.2$ clusters of 15–20% per Gyr.

4.2 The contribution of X-ray groups to the mass growth rate of clusters

Our finding of 39 *XMM*-detected galaxy groups in the infall regions of 23 massive clusters, corresponding to an average mass of $2.23 \times 10^{14} M_\odot$ per cluster, or 19% of the mean M_{200} mass of the primary cluster, suggests that these galaxy groups can explain a significant fraction of the mass growth of galaxy clusters between $z\sim 0.2$ and the present day.

The comparison sample of group-mass halos from the Millennium simulation allow us examine the likely fates of the 39 *XMM*-detected galaxy groups, by following the orbits from the $z=0.21$ snapshot where they are identified to the present day. We find that two-thirds (67%) of the simulated groups located within the *XMM* fields and recovered by the wavelet-reconstruction algorithm will be accreted into the cluster (pass within r_{200}) by the present day. In contrast, 22% of the detected *XMM* groups are expected to be physically more than $4 r_{200}$ from the cluster at the time of observation and despite being on their first infall, remain outside r_{200} at $z=0$. This is balanced by the 24% of those simulated infalling $M_{200} > 10^{13} M_\odot$ halos accreted into the clusters between $z=0.21$ and $z=0$ being outside the *XMM* field of view at $z=0.21$ and therefore missed from our sample. This can be understood given that those halos only accreted into the clusters in the last snapshot ($z < 0.02$) were on average at $2.89 \pm 0.70 r_{200}$ at $z=0.21$.

Taking the above correction factors into account, we estimate that clusters increase their mass by $16.2 \pm 4.2\%$ between $z=0.223$ and the present day (or 6% per Gyr) due to the accretion of groups more massive than $10^{13.2} M_\odot$. This confirms that X-ray groups are contributing significantly to the mass growth rate of clusters. However, this estimate for the mass accreted in the form of groups is only half that predicted for the overall mass growth of massive clusters over the same period (32–44%), as described in the previous section.

4.3 Accounting for the rest of the mass accreted by clusters and estimating their growth rates

Our empirical estimate that clusters are able to increase their masses by $\sim 16\%$ between $z=0.223$ and the present day through the accretion of $M_{200} > 10^{13.2} M_\odot$ X-ray groups is not sufficient to fully explain the mass growth rate of clusters. Thus, either the growth rate of massive clusters is much lower than that predicted by cosmological simulations, or there are other major contributions to the mass accretion rate of clusters from less massive DM halos (e.g. those hosting individual galaxies) or matter that is not bound within any DM halo.

Within the extended Press-Schechter (EPS) formalism (Press & Schechter 1974; Bond et al. 1991; Bower 1991; Lacey & Cole 1993), all of the growth of dark matter halos comes from mergers by construction. However, using merger trees constructed from both Millennium simulations, and taking care to accurately account for halo fragmentation, Genel et al. (2010) find that all resolved mergers, down to mass ratios of 10^{-5} between them contribute only $\approx 60\%$ of total halo mass growth, regardless of halo mass and redshift. Major mergers with ratios above 1:3 (1:10) contribute just 20% (30%). Instead they indicate that 40% of the mass in halos (up to and including cluster-mass halos) comes from genuinely smooth accretion of dark matter that was never bound in smaller halos. While there is some freedom of how merger trees are constructed, Genel et al. (2010) verified this result by following the individual dark matter particles within two cosmological simulations and labelling each one that had belonged to an identified bound structure at any point in its past, prior to its accretion into the primary halo.

Our estimate that the accretion of $M_{200} > 10^{13.2} M_\odot$ X-ray groups are sufficient to account for roughly 35–50% of the predicted mass growth rate of $\sim 10^{15} M_\odot$ clusters, appears consistent with the findings of Genel et al. (2010). This assumes that our L_X -based group mass estimates are unbiased relative to the true masses. Given their proximity to the primary cluster, some of these groups could be affected by ram-pressure stripping which progressively removes the X-ray emitting gas (see § 4.6). As a sanity check of our mass estimates, we split the groups into three mass bins, and for those groups with 4 or more confirmed members, measure the distribution of the LOS velocity offsets relative to the group's mean redshift. The resultant velocity dispersions are 257 km/s for the 12 groups with $\log M_{200} < 13.75$, 328 km/s for the 14 groups with $13.75 \leq \log M_{200} < 14.05$ and 369 km/s for the 7 groups with $\log M_{200} > 14.05$. These values are consistent with the $M_{200} - \sigma$ trend of SDSS groups (Yang et al. 2007) and the $L_X - \sigma$ relations of Zhang et al. (2011) and Clerc et al. (2016). The LOS velocity distributions of each stacked group sample are consistent with being a Gaussian function. Our sample may however miss the mass contribution from groups which have been recently accreted but are now orbiting back out beyond r_{200} . Their dark matter halo may still be largely intact, but the X-ray emitting gas has been sufficiently stripped as to be undetected. The LOS velocity offsets of such groups are likely to be rather low as they approach apocenter.

De Boni et al. (2016) have suggested that it is possible to estimate the overall mass accretion rate of clusters from their mass profiles beyond the virial radius. The aggregate radial velocity of dark matter within a radial shell reaches a minimum at $2-3 r_{200}$, that is beyond the splashback radius, and so most closely represents the infall of new material onto the cluster. By measuring the mass profile of the cluster over $2-3 r_{200}$ using the caustic method of Diaferio & Geller (1997), and assuming the infall velocity based on spherical collapse model, they are able to approximately reproduce the mass accretion rates of clusters within simulations. Given the current availability of dense redshift surveys of clusters galaxies beyond $2 r_{200}$ for many rich clusters (e.g. Rines et al. 2013), estimates of their typical mass accretion rates should be feasible.

4.4 The mass function of infalling X-ray groups

The variation of the DM halo mass function with large-scale density such that the MF appears top-heavy in overdense regions can be readily understood from a theoretical perspective. Collapsed DM halos are biased tracers of mass. This implies that the abundance of DM halos in overdense and underdense regions are not expected to simply differ by a factor which reflects the change in large-scale matter density. Instead:

$$n(M|\delta) \approx [1 + b(M, z)\delta] n(M) \quad (5)$$

where $n(M|\delta)$ is the abundance of DM halos of mass M in a region of overdensity δ , $n(M)$ is the cosmically averaged abundance, and $b(M, z)$ is the mass-dependent bias parameter of halos at redshift z (Mo & White 1996; Sheth & Tormen 1999; Abbas & Sheth 2005). As the bias $b(M)$ typically increases monotonically with mass (Tinker et al. 2010), this acts to increase the ratio of high-mass DM halos to low-mass halos in overdense regions, relative to less dense regions. Thus the mass function in overdense regions should be top-heavy. The effects of large-scale density on the halo mass function were examined by Faltenbacher, Finoguenov & Drory (2010) using the Millennium simulation, confirming that the fraction of matter within group-mass halos ($M_{200} \gtrsim 10^{13.5} M_{\odot}$) increases significantly with large-scale density, and the halo mass function becomes increasingly top heavy (see also Lemson & Kauffmann 1999).

Chon et al. (2013) found that clusters within superclusters were systematically more X-ray luminous than clusters outside superclusters. Assuming that this overabundance of X-ray luminous clusters represents an excess of massive clusters within superclusters, provides observational support for the theoretical expectation that the mass-function of clusters in overdense regions (superclusters) is top heavy. Similarly, this mass bias was also observed for galaxy groups in the vicinity of clusters in the 2dF Galaxy Redshift Survey (Ragone et al. 2004).

4.5 Impact for galaxy evolution

These X-ray groups are not only contributing a large proportion of the the dark matter required for cluster mass growth, but also host a significant fraction of the galaxies that arrive onto the clusters at late epochs. McGee et al. (2009) estimate that $\sim 50\%$ of cluster galaxies accreted since $z=0.5$ arrived onto the cluster as member of an infalling group with $M_{200} > 10^{13} M_{\odot}$. Galaxy groups have been shown to have a major impact on the evolution of their member galaxies, suppressing star formation activity through the interaction of the galaxy with the intra-group medium (ram-pressure stripping or starvation), or transforming their morphologies through low-velocity encounters and mergers with other group members. The fraction of star-forming galaxies among group members is lower than that seen in the field (at fixed stellar mass and redshift; Haines et al. 2007; Ziparo et al. 2014), and declines with increasing group mass and proximity to the group centre (Weinmann et al. 2006; Woo et al. 2013).

Thus, many galaxies are arriving onto clusters having already been transformed from star-forming spirals into passive early-types within groups, a mechanism known as pre-

processing (Zabludoff et al. 1996, 1998; Dressler et al. 2013; Just et al. 2015; Jaffé et al. 2016). This can contribute significantly to the cluster population of passive early-types, but also explain the short-fall of star-forming galaxies at large cluster-centric radii ($\gtrsim 2-3 r_{200}$) where no galaxies should have previously encountered the cluster (Chung et al. 2011; Haines et al. 2015). This should be exacerbated by the top-heavy mass function of these infalling groups, meaning that galaxies are more likely to be in massive X-ray luminous groups than the cosmic average. We will examine the impact of pre-processing on the galaxies within these infalling X-ray groups in Bianconi et al. (2017).

4.6 The next steps

This work presents a first attempt to quantify the numbers and demographics of X-ray groups in the immediate vicinity of a statistical sample of massive clusters, and derive empirical constraints on the rates at which clusters are growing through the accretion of group-mass systems. By identifying groups through their extended X-ray emission, we can confidently associate them to massive virialized DM halos. As we only have the X-ray luminosities of these groups, we have had to make certain simplifying assumptions to estimate their masses. In particular, by using the $M_{200} - L_X$ scaling relation of Leauthaud et al. (2010), we are assuming that the X-ray emitting gas content of these infalling groups remains bound within the host DM halo, and maintains the same density and temperature structures as isolated field groups (such as those from the COSMOS survey). At the same time, we expect that as these groups are accreted into the cluster, passing through the increasingly dense ICM, their X-ray emitting hot gas halos are progressively ram-pressure stripped (Gunn & Gott 1972; Poole 2006; McCarthy et al. 2008). The plasma physics of this process however very complex, with magnetic fields, turbulence, viscosity, KH instabilities and conduction all likely to play a role in determining when and how rapidly X-ray emitting gas is stripped from the group, the appearance of the extended tail of high-density stripped gas and how long this wake can survive before mixing with the ambient ICM (Roediger et al. 2015a,b).

Examples of this gas stripping have been seen in recent X-ray observations of groups infalling into Abell 85, Abell 2142, Abell 4067, ZwCl 8338 and Abell 780 (Ichinohe et al. 2015; Eckert et al. 2014; Chon & Böhringer 2015; Schellenberger & Reiprich 2005; De Grandi et al. 2016). These group-cluster mergers also leave shock fronts, spiral features indicative of gas sloshing and increased gas clumping in the cluster outskirts (Reiprich et al. 2013). On the other hand, during the group-cluster mergers, the X-ray luminosity may be briefly boosted as the group makes its pericenter passage (Ricker & Sarazin 2001), biasing the resulting group mass function (Randall, Sarazin & Ricker 2002). The hydrodynamical simulations of group-cluster mergers by Poole (2006) show how as a group approaches pericenter, the gas on its leading edge is heated and compressed, temporarily boosting its X-ray luminosity, before being steadily stripped, leaving an extended trail of cool, low-entropy gas behind it, similar to those seen by Eckert et al. (2014) and De Grandi et al. (2016). In particular, Eckert et al. (2014) estimate that $>90\%$ of the gas mass from the group falling into Abell 2142 has been stripped to form an 800 kpc long tail. These

detailed observations of individual group-cluster mergers are providing fundamental insights and constraints on the ICM plasma physics involved, revealing that the thermalization and mixing of the stripped group gas must be slow and inefficient (Eckert et al. 2017), and should lead to a better understanding of when and how the X-ray emitting gas is stripped from infalling groups.

The centres of an isolated group’s galaxy population, X-ray gas and DM halo should be coincident. As a group falls into a cluster, the ram pressure acts as a drag on the X-ray gas, causing it to lag behind the member galaxies and the dark matter, both of which are effectively collisionless. Hubble Space Telescope observations of these groups would allow their dark matter distributions to be constrained, to both confirm the overall masses of these groups and evidence of this lag in the hot gas component relative to the dark matter. Such observations can also test the self-interaction cross section of dark matter, which would create a drag on the dark matter within the infalling groups, displacing the DM distribution relative to the group galaxies (Harvey et al. 2014, 2015).

This *XMM* survey of infalling groups should also be a precursor to the much larger samples that should be obtained in the near future with eROSITA (Merloni et al. 2012). eROSITA will aim to perform a deep X-ray survey of the entire sky, with a combination of resolution and sensitivity good for studying the galaxy groups around $z < 0.1$ clusters. It will lead to large statistical improvements primarily on lower mass clusters, compared to the current sample, as the local volume is small. Also, in a combination with spectroscopic follow-up on 4MOST/VISTA it will deliver better statistics on larger separations from the cluster centre.

5 SUMMARY

We present an *XMM-Newton* survey to search for X-ray groups in the infall regions of 23 massive galaxy clusters at $0.15 \leq z < 0.30$ from the Local Cluster Substructure Survey (LoCuSS). All these clusters have excellent ancillary data including extensive spectroscopic coverage of cluster galaxies through the Arizona Cluster Redshift Survey (ACReS) and deep wide-field optical imaging from Subaru/Suprime-Cam, enabling us to identify the member galaxies associated with the X-ray emission of each group, and determine its redshift.

We identify 39 X-ray groups across the 23 *XMM* fields that have been spectroscopically confirmed to lie at the cluster redshift (and hence are likely falling into the primary cluster), above a signal-to-noise limit of 3. These groups all have at least one spectroscopic member, and a median of nine members. These infalling groups have M_{200} masses in the range $2 \times 10^{13} - 7 \times 10^{14} M_{\odot}$, based on estimates derived from their X-ray luminosities. The key results from a statistical analysis of these groups are:

- The 39 infalling X-ray groups lie at $0.28 - 1.35 r_{200}$ and are much more concentrated towards the cluster than the other 52 groups in the same fields (at the 6σ level). The distribution of the LOS velocity offsets of the infalling groups relative to the primary clusters is non-Gaussian, consistent with them being an infalling population.
- The comoving number density of the infalling X-ray groups is $\sim 25\times$ higher than that seen in field regions.

- The mass function of the infalling X-ray groups is top-heavy with respect to that seen for isolated groups in the XXL survey at the 3.5σ level. This is consistent with expectations of collapsed DM halos being biased tracers of the underlying large-scale density field.

- The average mass per cluster contained within these infalling X-ray groups is $2.2 \times 10^{14} M_{\odot}$, or $19 \pm 5\%$ of the mass of the primary cluster.

- We estimate that $\sim 10^{15} M_{\odot}$ clusters increase their masses by $16 \pm 4\%$ between $z=0.223$ and the present day due to the accretion of X-ray groups with $M_{200} \gtrsim 10^{13.2} M_{\odot}$. This represents 35–50% of the expected mass growth of these clusters at these late epochs. The rest of the mass growth is likely to occur through the smooth accretion of dark matter not bound within DM halos.

This work represents the first attempt to statistically establish the frequency and demographics of X-ray groups in the infall regions of a representative sample of massive clusters, estimate their contribution to the mass growth of clusters and mass function. It complements ongoing detailed X-ray studies examining the astrophysical processes acting on group-mass systems as they are accreted into massive clusters (e.g. Eckert et al. 2014; De Grandi et al. 2016).

ACKNOWLEDGMENTS

CPH acknowledges financial support from PRIN INAF 2014 and CONICYT Anillo project ACT-1122. GPS, MB, and FZ acknowledge support from the Science and Technology Facilities Council grant number ST/N000633/1.

REFERENCES

- Abbas U., Sheth R. K. 2005, MNRAS, 364, 1327
 Allen S.W., Evrard A.E., Mantz A.B., 2011, ARA&A, 49, 409
 Allevalo V. et al. 2012, ApJ, 758, 47
 Ascasibar Y., Diego J. M. 2008, MNRAS, 383, 369
 Beers T. C., Flynn K., Gebhardt K. 1990, AJ, 100, 32
 Behroozi P. S. et al. 2015, MNRAS, 454, 3020
 Bianconi M. et al. 2017, MNRAS submitted
 Böhringer H. et al. 2004, A&A, 425, 367
 Böhringer H., Chon G., Collins C.A. 2014, A&A, 570, 31
 Bonamente M., Landry D., Maughan B., Giles P., Joy M., Nevalainen J. 2013, MNRAS, 428, 2812
 Bond J.R., Cole S., Efstathiou G., Kaiser N., 1991, ApJ, 379, 440
 Bower R.G., 1991, MNRAS, 248, 332
 Boylan-Kolchin M., Springel V., White S.D.M., Jenkins A., Lemson G., 2009, MNRAS, 398, 1150
 Correa C. A., Wyithe S. B., Schaye J., Duffy A. R., 2015, MNRAS, 450, 1514
 Chon G., Böhringer H., Smith G. P. 2012, A&A, 548, 59
 Chon G., Böhringer H., Nowak N. 2013, MNRAS, 429, 3272
 Chon G., Böhringer H., 2015, A&A, 574, 132
 Chung S. M. et al. 2011, ApJ, 743, 34
 Clerc N. et al. 2016, MNRAS, 463, 4490
 Czoske O. 2004, in IAU Colloq. 194, Outskirts of Galaxy Clusters: Intense Life in the Suburbs, ed. A. Diaferio (Cambridge: Cambridge Univ. Press), 183

- David L. P., Kempner J. 2004, *ApJ*, 613, 831
- De Boni C., Serra A., Diaferio A., Giocoli C., Baldi M. 2016, *ApJ*, 818, 188
- De Grandi S. et al. 2016, *A&A*, 592, 154
- Diaferio A., Geller M. J., 1997, *ApJ*, 481, 633
- Dressler A., Oemler A. Jr., Poggianti B., Gladders M. D., Abramson L., Vulcani B. 2013, *ApJ*, 770, 62
- Dutton A.A., Macciò A.V., 2014, *MNRAS*, 441, 3359
- Ebeling H. et al. 1998, *MNRAS*, 301, 881
- Ebeling H. et al. 2000, *MNRAS*, 318, 333
- Eckert D. et al. 2014, *A&A*, 570, 119
- Eckert D. et al. 2017, preprint (arXiv:1705.05844)
- Edwards L. O. V., Fadda D., Frayer D. T., Lima Neto G. B., Durret F. 2010, *ApJ*, 140, 1891
- Eisenstein D. J., Hu W., 1998, *ApJ*, 496, 605
- Fadda D., Biviano A., Marleau F. R., Storrie-Lombardi L. J., Durret F. 2008, *ApJL*, 672, 9
- Fakhouri O., Ma C.-P., 2008, *MNRAS*, 386, 577
- Fakhouri O., Ma C.-P., Boylan-Kolchin M., 2010, *MNRAS*, 406, 2267
- Faltenbacher A., Finoguenov A., Drory N. 2010, *ApJ*, 712, 484
- Finoguenov A. et al. 2007, *ApJS*, 172, 182
- Finoguenov A. et al. 2009, *ApJ*, 704, 564
- Finoguenov A. et al. 2010, *MNRAS*, 403, 2063
- Finoguenov A. et al. 2015, *A&A*, 574, 130
- Forman W. et al. 1981, *ApJL*, 243, 133
- Frenk C. S. et al. 1999, *ApJ*, 525, 554
- Gao L., Navarro J.F., Frenk C.S., Jenkins A., Springel V., White S.D.M., 2012, *MNRAS*, 425, 2169
- Gehrels N., 1986, *ApJ*, 303, 336
- Genel S., Bouché N., Naab T., Sternberg A., Genzel R., 2010, *ApJ*, 719, 229
- Giles P. A., Maughan B. J., Birkinshaw M., Worrall D. M., Lancaster K., 2012, *MNRAS*, 419, 503
- Giocoli C., Tormen G., van den Bosch F. C., 2008, *MNRAS*, 386, 2135
- Giocoli C., Tormen G., Sheth R. K., van den Bosch F. C., 2010, *MNRAS*, 404, 502
- Governato F., Babul A., Quinn T., Tozzi P., Baugh C.M., Katz N., Lake G. 1999, *MNRAS*, 307, 949
- Gunn J. E., Gott J. R. 1972, *ApJ*, 176, 1
- Gutierrez K., Krawczynski H., 2005, *ApJ*, 619, 161
- Haines et al., 2007, *MNRAS*, 381, 7
- Haines et al., 2009a, *ApJ*, 704, 126
- Haines et al., 2009b, *MNRAS*, 396, 1297
- Haines et al., 2010, *A&A*, 518, L19
- Haines et al., 2012, *ApJ*, 754, 97
- Haines et al., 2013, *ApJ*, 775, 126
- Haines et al., 2015, *ApJ*, 806, 101
- Harvey D. et al. 2014, *MNRAS*, 441, 404
- Harvey D. et al. 2015, *Sci*, 347, 1462
- Henry J. P., Evrard A. E., Hoekstra H., Babul A., Mahdavi A. 2009, *ApJ*, 691, 1307
- Hikage C., Yamamoto K., 2016, *MNRAS*, 455, L77
- Ichinohe Y. et al. 2015, *MNRAS*, 448, 2971
- Jaffé Y. L. et al. 2016, *MNRAS*, 461, 1202
- Jiang F., van den Bosch F. C., 2014, *MNRAS*, 440, 193
- Jones C., Forman W., 1999, *ApJ*, 511, 65
- Just D. W. et al. 2015, preprint (arXiv:1506.02051)
- Kettula K. et al. 2015, *MNRAS*, 451, 1460
- Kravtsov A.V., Borgani S., 2012, *ARA&A*, 50, 353
- Lacey C. G., Cole S., 1993, *MNRAS*, 262, 627
- Leauthaud A. et al., 2010, *ApJ*, 709, 97
- Lemson G., Kauffmann G., 1999, *MNRAS*, 302, 111
- Lemze D. et al., 2013, *ApJ*, 776, 91
- Lovisari L., Reiprich T. H., Schellenberger G., 2015, *A&A*, 573, 118
- Mahdavi A., Hoekstra H., Babul A., Bildfell C., Jeltema T., Henry J. P. 2013, *ApJ*, 767, 116
- Mann A. W., Ebeling H., 2012, *MNRAS*, 420, 2120
- Mantz A., Allen S.W., Rapetti D., Ebeling H., 2010, *MNRAS*, 406, 1759
- Martinet N. et al. 2016, *A&A*, 590, 69
- Martino R. et al. 2014, *MNRAS*, 443, 2342
- McBride J., Fakhouri O., Ma C.-P., 2009, *MNRAS*, 398, 1858
- McCarthy I. G. et al. 2008, *MNRAS*, 383, 593
- McCarthy I. G., Schaye J., Bird S., Le Brun A. M. C. 2017, *MNRAS*, 465, 2936
- McGee S. L., Balogh M. L., Bower R. G., Font A. S., McCarthy I. G. 2009, *MNRAS*, 400, 937
- Merloni A. et al. 2012, preprint (arXiv:1209.3314)
- Mo H. J., White S. D. M. 1996, *MNRAS*, 282, 347
- Okabe N., Umetsu K. 2008, *PASJ*, 60, 345
- Okabe N., Takada M., Umetsu K., Futamase T., Smith G.P., 2010, *PASJ*, 62, 811
- Okabe N., Smith G. P., Umetsu K., Takada M., Futamase T. 2013, *ApJL*, 769, 35
- Okabe N., Futamase T., Kajisawa M., Kuroshima R. 2014, *ApJ*, 784, 90
- Okabe N., Smith G. P., 2016, *MNRAS*, 461, 3794
- O'Sullivan E. et al. 2017, preprint (arXiv:1708.03555)
- Pacaud F. et al. 2016, *A&A*, 592, 2
- Pearson R. et al. 2017, *MNRAS*, 469, 3489
- Pedersen K., Dahle H., 2007, *ApJ*, 667, 26
- Pereira M. J. et al. 2010, *A&A*, 518, L40
- Pierre M. et al. 2016, *A&A*, 592, 1
- Planck Collaboration et al., 2014a, *A&A*, 571, 20
- Planck Collaboration et al., 2014b, *A&A*, 571, 16
- Planck Collaboration et al., 2016, *A&A*, 594, 13
- Poole G. B., Fardal M. A., Babul A., McCarthy I. G., Quinn T., Wadsley J. 2006, *MNRAS*, 373, 881
- Press W.H., Schechter P., 1974, *ApJ*, 187, 425
- Ragone C. J., Merchán M., Muriel H., Zandivarez A., 2004, *MNRAS*, 350, 983
- Randall S. W., Sarazin C. L., Ricker P. M. 2002, *ApJ*, 577, 579
- Reiprich T. H. et al. 2013, *Space Science Reviews*, 177, 195
- Ricker P., Sarazin C. L. 2001, *ApJ*, 561, 621
- Rines K., Geller M. J., Diaferio A., Kurtz M. J. 2013, *ApJ*, 767, 15
- Rizza E., Burns J. O., Ledlow M. J., Owen F. N., Voges W., Bliton M. 1998, *MNRAS*, 301, 328
- Roediger E. et al. 2015a, *ApJ*, 806, 103
- Roediger E. et al. 2015b, *ApJ*, 806, 104
- Sanderson A. J. R., Ponman T. J. 2010, *MNRAS*, 402, 65
- Schellenberger G., Reiprich T. H., 2015, *A&A*, 583, L2
- Schuecker P., Böhringer H., Collins C.A., Guzzo L., 2003, *A&A*, 398, 867
- Scoville N. et al. 2007, *ApJS*, 172, 1
- Sheth R. K., Tormen G. 1999, *MNRAS*, 308, 119
- Smith G. P. et al. 2005, *MNRAS*, 359, 417
- Smith G. P. et al. 2010, *A&A*, 518, L18

- Smith G. P. et al. 2016, MNRAS, 456, L74
Spergel D. N., et al. 2003, ApJS, 148, 175
Springel V. et al. 2005, Nature, 435, 629
Taylor J. E., Babul A. 2005, MNRAS, 364, 515
Tinker J. L. et al. 2010, ApJ, 724, 878
van den Bosch F. C., Tormen G., Giocoli C., 2005, MNRAS, 359, 1029
van den Bosch F. C., Jiang F., Hearin A., Campbell D., Watson D., Padmanabhan N., 2014, MNRAS, 445, 1713
Vikhlinin A., McNamara B. R., Forman W., Jones C., Quintana H., Hornstrup A., 1998, ApJ, 502, 558
Vikhlinin A. et al., 2009, ApJ, 692, 1060
Voit G. M., 2005, Rev. Modern Phys., 77, 207
Weinmann S. M., van den Bosch F. C., Yang X., Mo H. J. 2006, MNRAS, 366, 2
Woo J. et al. 2013, MNRAS, 428, 3306
Xu L., Rieke G. H., Egami E., Pereira M. J., Haines C. P., Smith G. P., 2015a, ApJS, 219, 18
Xu L., Rieke G. H., Egami E., Haines C. P., Pereira M. J., Smith G. P., 2015b, ApJ, 808, 159
Yang X. et al. 2007, ApJ, 671, 153
Yang X., Mo H. J., Zhang Y., van den Bosch F. C., 2011, ApJ, 741, 13
Zabludoff A. I. et al. 1996, ApJ, 466, 104
Zabludoff A. I. & Mulchaey J. S. 1998, ApJ, 496, 39
Zentner A. R., Bullock J. S., 2003, ApJ, 598, 49
Zhang Y.-Y. et al. 2007, A&A, 467, 437
Zhang Y.-Y. et al. 2011, A&A, 526, 105
Zhao D.H., Jing Y.P., Mo H.J., Börner G., 2009, ApJ, 707, 354
Ziparo F. et al. 2014, MNRAS, 437, 458

This paper has been typeset from a \TeX / \LaTeX file prepared by the author.